Journal of Nanobiotechnology

RESEARCH Open Access

Designing highly stable ferrous selenide-black phosphorus nanosheets heteronanostructure via P-Se bond for MRI-guided photothermal therapy

Xuanru Deng[1†], Hongxing Liu[1,2,3†], Yuan Xu[2], Leung Chan[1,2], Jun Xie[1], Zushuang Xiong[1], Zheng Tang[1], Fang Yang[1*] and Tianfeng Chen[1,2*]

Abstract

Background: The design of stable and biocompatible black phosphorus-based theranostic agents with high photothermal conversion efficiency and clear mechanism to realize MRI-guided precision photothermal therapy (PTT) is imminent.

Results: Herein, black phosphorus nanosheets (BPs) covalently with mono-dispersed and superparamagnetic ferrous selenide ($FeSe_2$) to construct heteronanostructure nanoparticles modified with methoxy poly (Ethylene Glycol) (mPEG-NH_2) to obtain good water solubility for MRI-guided photothermal tumor therapy is successfully designed. The mechanism reveals that the enhanced photothermal conversion achieved by BPs-$FeSe_2$-PEG heteronanostructure is attributed to the effective separation of photoinduced carriers. Besides, through the formation of the P-Se bond, the oxidation degree of $FeSe_2$ is weakened. The lone pair electrons on the surface of BPs are occupied, which reduces the exposure of lone pair electrons in air, leading to excellent stability of BPs-$FeSe_2$-PEG. Furthermore, the BPs-$FeSe_2$-PEG heteronanostructure could realize enhanced T_2-weighted imaging due to the aggregation of $FeSe_2$ on BPs and the formation of hydrogen bonds, thus providing accurate PTT guidance and generating hyperthermia to inhabit tumor growth under NIR laser with negligible toxicity in vivo.

Conclusions: Collectively, this work offers an opportunity for fabricating BPs-based heteronanostructure nanomaterials that could simultaneously enhance photothermal conversion efficiency and photostability to realize MRI-guided cancer therapy.

Keywords: Black phosphorus, P-se bond, Heteronanostructure, MRI, Photothermal therapy

Background

The incidence of malignant tumors is increasing, which is one of the major diseases leading to human death [1]. Great efforts have been devoted to combating cancer, and traditional treatments such as chemotherapy, radiotherapy, and surgical resection have been developed [2]. However, therapeutic effects are not always satisfactory because of the metastasis and invasiveness of cancer. PTT relies on photothermal reagents to absorb near-infrared

*Correspondence: tyoung@jnu.edu.cn; tchentf@jnu.edu.cn
†Xuanru Deng and Hongxing Liu contributed equally to this work
[1] College of Chemistry and Materials Science, Guangdong Provincial Key Laboratory of Functional Supramolecular Coordination Materials and Applications, Jinan University, Guangzhou 510632, China
Full list of author information is available at the end of the article

light to convert high temperature to achieve tumor ablation. Owing to the noninvasive, slight side effect and high temporal specificity, in recent years, PTT has attracted extensive attention. Therefore, it is necessary to find an efficient photothermal reagent to improve the effect of photothermal therapy. Generally, PTT reagents are divided into organic photothermal nanomaterials and inorganic nanomaterials [3–8]. Organic nanomaterials such as indocyanine green (ICG) [9], conjugated polymers [10] and dopamine melanin [11], have high biocompatibility and low toxicity, but poor photobleaching and thermal stability hinder their application in biomedicine. In contrast, inorganic nanomaterials such as graphene oxide [12], precious metal nanomaterials [13], transition metal carbides [14] and carbonitrides [15, 16] have been widely researched due to their easy modification, adjustable morphology and high physiological stability [17, 18]. However, the safety and biocompatibility of inorganic nanomaterials are still great challenges. Therefore, the design and search for photothermal reagents with safety, good stability, high photothermal conversion and good biocompatibility remain significant challenges.

Among the photothermal reagents, BPs, as emerging two-dimensional materials [19, 20], have unique properties such as huge surface area [21], high photothermal conversion efficiency [22], good biocompatibility [23] and eventual degradation to non-toxic phosphate or phosphonate, which have attracted increasing attention from researchers. Thus, BPs have been widely studied in antibacterial [24, 25], wound healing [26], antitumor [27–31] and other diseases [32, 33]. However, the lone pair electrons on the surface of BPs lead to high reactivity in air and water [34], which hindered the application of BP-based nanomaterials in the biomedical area. Fortunately, researchers have developed a wide range of strategies to functionalize the BPs surface to improve the stability, including the formation of solvent shells in the stripping process [35], surface coverage of two-dimensional materials[36], edge-selective functionalization [37] and oxide layer passivation [38]. Although these methods have achieved good results in improving the stability of black phosphorus, their biomedical applications are limited due to the complexity of preparation methods and unclear functional mechanism. Besides, designing therapeutic nanoparticles with MRI ability is significant for accurate cancer treatment. MRI provides a wealth of tumor information for pre-treatment diagnosis and a basis for real-time monitoring therapeutic progression to judge the curative effect. Some researchers have recently combined black phosphorus with MRI contrast reagents to build an integrated platform for theranostics. BPs were coated with tannic acid to chelate with Mn^{2+} ions, endowing the theranostic nanoplatform with T_1 MRI-guided PTT ability [32, 39]. In other studies, BPs were loaded with Ce6 [40], Fe_3O_4 [41], MnO_2 [42] and upconversion nanoparticles [43] to achieve imaging-guided PTT and PDT. Although black phosphorus nanoplatforms have been endowed with imaging ability [44] and improved photothermal conversion efficiency by the above strategies, the mechanism of enhanced photothermal conversion efficiency or degradability of nanomaterial was rarely clarified. Therefore, it is necessary to design BP-based nanoparticles with clear mechanisms, good degradability and MRI ability to combat cancer.

Fe and Se belong to biofriendly elements [45]. Fe-containing nanoparticles have been widely studied in MRI [46–48]. $FeSe_2$, as a crucial class of transition metal dichalcogenide, has attracted intensive interest because of its excellent magnetic properties [49], good electrical conductivity [50] and high absorbance in the near-infrared (NIR) region [51]. However, $FeSe_2$ contains Fe^{2+}, which is easily oxidized to Fe^{3+} in vivo and in vitro [52]. We hypothesized that the lone pair electrons on the surface of black phosphorus could covalently combine with $FeSe_2$ to improve each other's stability. Besides, our previous studies have shown that BPs heteronanostructure materials could improve radiosensitization efficiency by increasing the chance of energy transfer [53, 54]. Therefore, we speculate that BPs are covalently bonded with $FeSe_2$ to form heteronanostructure, which could improve the photothermal conversion efficiency and stability while facilitating T_2 imaging.

Herein, we designed and synthesized P-Se bonded BPs-$FeSe_2$ heteronanostructure imaging therapeutic system as an efficient and stable photothermal reagent and MRI reagent to achieve T_2-weighted imaging-guided PTT in Scheme 1. The benefit of the therapeutic system is the integration of the treatment function with MRI for precise treatment. Superior to previous studies, the as-prepared BPs-$FeSe_2$-PEG heterostructures displayed higher photothermal conversion than free $FeSe_2$-PEG or BPs-PEG upon NIR laser irradiation because the heterostructure enhanced the effective separation of photoinduced electrons and holes and reduced the recombination rate of photoinduced carriers. Photoinduced electrons and holes could be converted to hot carriers under irradiation, and then generate phonons to release the excess energy to return to equilibrium state via non-radiative recombination at the interface of $FeSe_2$ and BPs. The excess energy caused enhanced photothermal performance of BPs-$FeSe_2$ than that of single $FeSe_2$ or BPs. Moreover, BPs-$FeSe_2$-PEG heterostructure with MRI ability was acquired because of the superparamagnetism ability of $FeSe_2$. Therefore, rational design of BPs-$FeSe_2$-PEG heterostructures

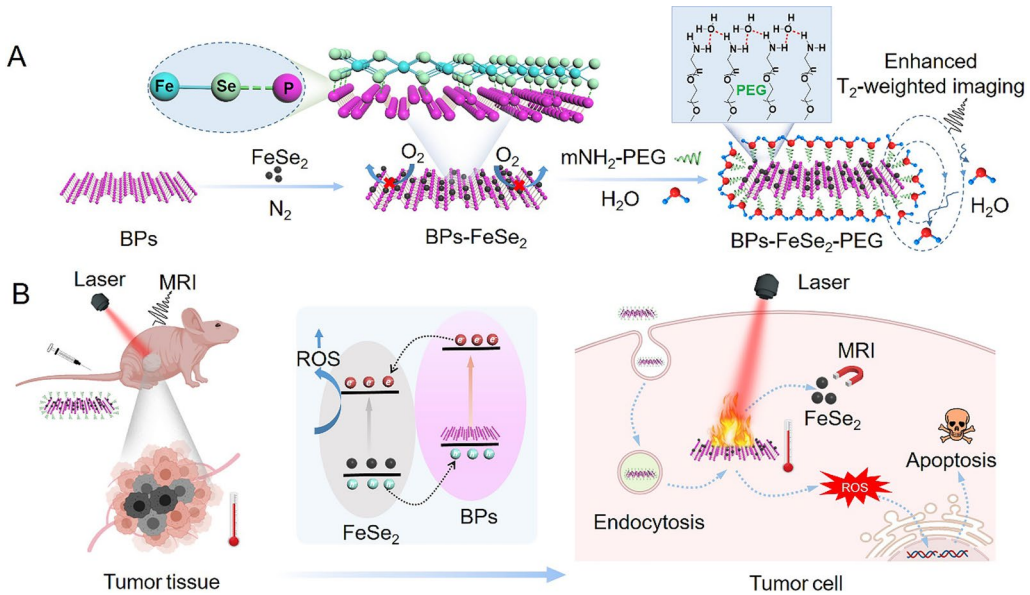

Scheme 1 The schematic illustration of BPs-$FeSe_2$-PEG heteronanostructure as MRI-guided agent for PTT. **A** the synthesis of BPs-$FeSe_2$-PEG heteronanostructure. **B** the application and mechanism of BPs-$FeSe_2$-PEG heteronanostructure as MRI-guided PTT agent

could simultaneously improve the deficiency of BPs and achieve the following advantages: (i) Photothermal stability of BPs-$FeSe_2$-PEG is improved because of the formation of P-Se covalent bond. The oxidation degree of $FeSe_2$ is weakened and the lone pair electrons on the surface of black phosphorus are occupied, which reduces the exposure of lone pair electrons in air to prevent the oxidation, leading to the excellent stability of BPs-$FeSe_2$-PEG; (ii) Mechanism research shows that the BPs-$FeSe_2$-PEG heteronanostructure presents enhanced photothermal conversion efficiency ($\eta = 26.7\%$). In addition, ROS generation ability was also improved. These results were ascribed to the enhanced separation of photoinduced electrons and holes and the reduced recombination rate of photoinduced carriers during the formation of heterostructure; (iii) BPs-$FeSe_2$-PEG could act as T_2 MRI contrast agent to realize MRI-guided precision photothermal treatment of cancer. Besides, the BPs-$FeSe_2$-PEG heteronanostructure could realize enhanced T_2-weighted imaging due to the aggregation of $FeSe_2$ on the surface of BPs and the formation of hydrogen bonds; (iv) Owing to the excellent thermal ablation effect, the therapeutic strategy of BPs-$FeSe_2$-PEG combined with NIR irradiation shows a powerful antitumor ability; and (v) The nanomedicine has the characteristics of good degradability and no observable toxicity to major organs. Taken together, BPs-$FeSe_2$-PEG heterostructures have great clinical potential for MRI-guided precision photothermal therapy.

Materials and methods

Materials

Bulk BP, N-Methyl pyrrolidone (NMP), ethanol, 1-ethyl-3-[3-(dimethylamino)-propyl] carbodiimide hydrochloride (EDC) and N-hydroxysuccinimide (NHS), cyclohexane, thiazolyl blue tetrazolium bromide (MTT), propidium iodide (PI) were obtained from Sigma-Aldrich. Oleyl amine, 1-Octadecene, Methoxy Polyethylene Glycol Amine and Poly (acrylic acid) (PAA) (M.W ~ 2000) were obtained from Macklin. $FeCl_24H_2O$ was obtained from Aladdin.

Preparation BPs

Bulk BP (50 mg) was mixed with NMP solution (200 mL) and ultrasonic (960 W) for different times (8, 10 and 12 h) to obtain BPs with different thicknesses. The solution was then centrifuged (5000 rpm, 10 min) to remove the bulk BP crystals. The supernatant was centrifuged (8000 rpm, 10 min) to separate thick black phosphorus slices. Finally, the obtained supernatant was centrifuged (12,000 rpm, 60 min). The precipitate was washed with ethanol two times and stored in ethanol (20 mL) at 4 °C.

Preparation of $FeSe_2$

$FeSe_2$ were synthesized according to previously reported method [55]. Under the N_2 conditions, oleylamine

(15 mL) and 1-octadecene (10 mL) were mixed in a three-necked flask and then maintained at 120 °C for 30 min. $FeCl_24H_2O$ (1 mmol) was rapidly added to the solution and kept at 120 °C. Simultaneously, the solution was intensely stirred for 30 min. Selenium powder (2 mmol) and oleylamine (4 mL) were mixed and heated under the condition of N_2 until dissolved. The dissolved selenium powder was slowly injected into the flask. The temperature was rapidly raised to 150 °C in 10 min and maintained for 30 min. The reaction was cooled to room temperature under the N_2 condition. The excess cyclohexane was added to the solution. Then the solution was centrifuged to obtain precipitate. Finally, the precipitate was dissolved in absolute ethyl alcohol and stored under the condition of N_2.

Preparation of $FeSe_2$-PEG

$FeSe_2$ ethanol solution was slowly added to the excess PAA solution under ultrasound. The excess ethanol and PAA were removed by centrifugation (8000 rpm, 5 min). Subsequently, the excess mPEG-NH_2 solution was added to the PAA-$FeSe_2$ aqueous solution. Then 5 mg EDCNHS was added to the $FeSe_2$-PEG solution, stirred overnight at room temperature. $FeSe_2$-PEG was collected by centrifugation (8000 rpm, 15 min). The obtained $FeSe_2$-PEG was suspended in water.

Preparation of BPs-PEG

10 mg mPEG-NH_2 was dispersed in 10 mL 200 μg/mL BPs aqueous solution under ultrasound. The resulting BPs-PEG were centrifugated at 4000 rpm for 30 min and washed twice. The obtained BPs-PEG was dissolved in ultrapure water.

Preparation of BPs-$FeSe_2$-PEG

3 mL of 4 mg/mL $FeSe_2$ ethanol solution was slowly added to 3 mL of 1 mg/mL BPs ethanol solution ($FeSe_2$: BPs 4:1), stirred for 12 h in the dark and centrifuged to remove the supernatant (3000 rpm, 15 min). Subsequently, the excess mPEG-NH_2 solution was added to the solution and stirred overnight. The solution was then centrifuged to remove the supernatant (3000 rpm, 20 min). The obtained BPs-$FeSe_2$-PEG was dissolved in water.

Preparation of various $FeSe_2$: BPs ratios of BPs-$FeSe_2$-PEG

$FeSe_2$ ethanol solution (1 mg/mL) was slowly added to 1 mg/mL of BPs ethanol solution with different ratio ($FeSe_2$: BPs 5:1, 4:1, 2:1, 1.5:1 and 1:1), stirred for 12 h in the dark and centrifuged to remove the supernatant (3000 rpm, 15 min). Subsequently, the excess mPEG-NH_2 solution was added to the solution and stirred overnight. The solution was then centrifuged to remove the supernatant (3000 rpm, 20 min). The obtained BPs-$FeSe_2$-PEG was dissolved in water.

Characterization of the BPs-$FeSe_2$-PEG

The morphologies of $FeSe_2$, BPs and BPs-$FeSe_2$ were determined by transmission electron microscopy (TEM), high-resolution TEM and atomic force microscope (AFM). The structures of $FeSe_2$, BPs and BPs-$FeSe_2$ were measured by X-ray photoelectron spectroscopy (XPS), X-ray powder diffraction (XRD), UV–vis-NIR spectrophotometry and Raman scattering. The elemental distributions of BPs-$FeSe_2$ were characterized by energy-dispersive X-ray spectroscopy (EDS).

Stability of nanoplatforms

The UV–vis absorbance of the $FeSe_2$-PEG, BPs-PEG and BPs-$FeSe_2$-PEG dispersed in ultrapure water (pH = 7) were monitored at 0, 1, 2, 3, 4 and 5 days.

Photothermal effects of nanoplatforms

To evaluate the effects of PEGylated $FeSe_2$, BPs and BPs-$FeSe_2$ used as photothermal agents, first, an equivalent concentration of PEGylated $FeSe_2$, BPs and BPs-$FeSe_2$ (120 μg/mL) were illuminated with different laser (0.5, 1, 1.5, 2 W/cm^2). Second, a range of concentrations of PEGylated $FeSe_2$, BPs and BPs-$FeSe_2$ solution (600 μL) including 15, 30, 60 and 120 μg/mL were irradiated by NIR laser at 1.5 W/cm^2 for 10 min.

The photothermal conversion efficiency of nanoplatforms

PEGylated $FeSe_2$, BPs and BPs-$FeSe_2$ (1 mL) were added to the ultraviolet quartz dish. The photothermal conversion efficiency (η) of the cooling stage as measured through the following formula:

$$\eta = \frac{h\,s\Delta T_{max} - Q_s}{I\left(1 - 10^{-A_{808}}\right)}$$

where (mW/$m^{2\circ}$C) represents the heat transfer coefficient, S(m^2) means the surface area of the ultraviolet quartz dish, ΔT_{max} refers to the difference between the equilibrium and the ambient temperature. Q_s is equal to the heat absorbed from the light by the ultraviolet quartz vessel containing water. I stands for the laser power density. A_{808} means the absorbance at 808 nm. s = m c/T, where m refers to the solution mass, c means the specific heat capacity of the solution, and T is the ratio of time to − Inθ in the cooling process. $FeSe_2$-PEG, BPs-PEG and

BPs-$FeSe_2$-PEG were added into ultraviolet quartz dishes, respectively.

Degradation of nanoplatforms

The $FeSe_2$-PEG, BPs-PEG and BPs-$FeSe_2$-PEG (1 mg/mL, 1 mL) were suspended in PBS solution at pH 5.3, pH 5.3 with 1 mg/mL lysozyme, pH 7.4 and EJ cells lysates in RIPA with or without laser. The morphology changes of nanoplatforms were recorded by TEM.

Magnetic properties of BPs-$FeSe_2$-PEG

The magnetic properties of $FeSe_2$-PEG and BPs-$FeSe_2$-PEG solution of different concentrations (0, 0.00125, 0.0025, 0.005, 0.01 and 0.02 mM) were recorded T_2-weighted images by 1.5 T clinical MRI system (Signa HDxt, Milwaukee, WI).

Cell culture

The human urinary bladder carcinoma cells EJ cells were purchased from American Type Culture Collection (ATCC, Manassas, Virginia, USA). EJ cells were cultured in DMEM medium with fetal bovine serum (10%), penicillin (100 units/mL), and streptomycin (50 units/mL) in a humidified incubator at 37 °C with 5% CO_2 atmosphere.

Anticancer efficacy of nanoplatforms

A range of concentration (from 0 to 50 μg/mL) of PEGylated $FeSe_2$, BPs and BPs-$FeSe_2$ incubated with EJ cells (density of 2×10^4/mL, 100 μL) in the 96-hole wells for 8 h. The laser groups cells were exposed to laser (1.5 W/cm^2, 5 min) and incubated for another 64 h. MTT solution was added to the cells. Then the supernatant was extracted and added 150 μL DMSO to each well. The absorption was measured at 570 nm by a microplate reader.

Calcein-AM and PI staining

EJ cells incubated with PEGylated $FeSe_2$, BPs and BPs-$FeSe_2$ (25 μg/mL) for 8 h. The cells were irradiated with NIR laser (1.5 W/cm^2, 5 min). The supernatant was removed. The same volume of PBS was added. The AM and PI were used to detect living cells and dead cells, respectively. Finally, the living and dead cells were recorded by fluorescence microscopy.

Cellular uptake

Coumarin 6-labeled PEGylated $FeSe_2$, BPs and BPs-$FeSe_2$ were prepared to quantify the uptake of nanomaterials in cells. EJ cells were seeded at 6-well plates and incubated for 24 h. The same concentration of PEGylated $FeSe_2$, BPs and BPs-$FeSe_2$ (25 μg/mL) were added to EJ cells and incubated for 0, 1, 2, 4, 8 and 12 h. Next, the cells were collected and measured by flow cytometry [56].

Intracellular localization of BPs-$FeSe_2$-PEG in EJ cells

Lysosomes and nucleus were stained with lysotracker and DAPI, respectively. BPs-$FeSe_2$-PEG was incubated with EJ cells for 0, 1, 2, 4, 8 and 12 h. The fluorescence was capture by a fluorescence microscope (EVOS FL Auto Imaging System, AMAFD1000).

Flow cytometric analysis

EJ cells were incubated with the same concentration of PEGylated $FeSe_2$, BPs and BPs-$FeSe_2$ (25 μg/mL) for 8 h. The laser irradiation groups were exposed to laser (1.5 W/cm^2, 5 min). All of the groups were incubated for 72 h in total and stained with PI. Finally, the cells were analyzed by a flow cytometer.

Annexin V-FITC and PI staining

EJ cells were incubated with PEGylated $FeSe_2$, BPs and BPs-$FeSe_2$ (25 μg/mL) for 8 h. The laser groups were exposed to the laser (1.5 W/cm^2, 5 min). All of the groups were incubated for 72 h in total. The cells were collected by centrifugation and resuspended in 300 μL binding buffer. Finally, the cells were stained with Annexin V-FITC and PI according to the kit method and analyzed by a flow cytometer.

Intracellular hydrogen peroxide and $^1O_2$ generation

EJ cells were incubated with 100 μg/mL of PEGylated $FeSe_2$, BPs and BPs-$FeSe_2$. The cells with or without laser (1.5 W/cm^2, 1 min) were treated with DCFH-DA or 1, 3-diphenylisobenzofuran (DPBF) at a final concentration of 10 μM and 20 μM, respectively. Intracellular hydrogen peroxide and $^1O_2$ generation were detected as the fluorescence intensity.

MRI of BPs-$FeSe_2$-PEG in vivo

$FeSe_2$-PEG and BPs-$FeSe_2$-PEG were intravenously injected (10 mg/kg). The T_2-weighted signal of $FeSe_2$ in tumor regions was collected at different time points (0, 2, 6, 12, 24 h) by a 3.0 T MR scanner (Bruker Biospin Corporation, Billerica, MA, USA).

Antitumor activity in vivo

The nude mice used in this study were purchased from Beijing Vital River Laboratory Animal Technology Co, Ltd. All animal experiments were conducted under the approval of the Animal Experimentation Ethics Committee of Jinan University. 1×10^7 EJ cells were suspended in

100 μL DMEM hypodermic and injected into nude mice. When the tumor reached about 120–150 mm^3, the mice were intravenously injected with $FeSe_2$-PEG, BPs-PEG and $FeSe_2$-BPs-PEG (10 mg/kg). After 2 h of administration, the tumors of laser groups were irradiated with 808 nm laser (1.5 W/cm^2, 10 min). The control mice were injected with an equal volume of saline. The tumor volume and body weight of each mouse was recorded per 2 days. The main organs, blood and tumors were collected after 21 days.

Photothermal imaging in vivo

When the tumor volume of the nude mice reaches 150 mm^3, the nude mice were randomly divided into four groups. PEGylated $FeSe_2$, BPs and BPs-$FeSe_2$ (10 mg/kg) are injected via intravenous. Then the temperature and images of the tumor area under laser irradiation (1.5 W/cm^2, 10 min) were recorded by the infrared imager.

Evaluation of antitumor effects by MRI

The nude mice of all groups were recorded the MRI images of tumor regions at 21 days of treatments by a 9.4 T MRI scanner. The necrotic degree of tumor issues was evaluated by the indexes of standard ADC, fast ADC and slow ADC.

Pharmacokinetic study of BPs-$FeSe_2$-PEG

Three female SD mice (180–200 g) were intravenously injected BPs-$FeSe_2$-PEG (4 mg/kg). Then we collected the blood from the eyes at 0.5, 1, 2, 4, 8, 12, 24, 48 and 72 h, respectively. We obtained the serum by centrifugation. Then the serum was digested with chloroazotic acid. The content of Se was determined by inductively coupled plasma mass spectrometry (ICP-MS).

Statistical and synergy analysis

Statistical analysis was performed using the SPSS statistical program version 13 (SPSS Inc. Chicago, IL). All the experiments were carried out at least in triplicate. The results were expressed as means ± SD. Differences between the two groups were analyzed by the two-tailed Students *t*-test. Differences of $P < 0.05$ (*), $P < 0.01$ (**) *or* $P < 0.001$ (***) was indicated.

Results and discussion

Preparation and characterization of BPs-$FeSe_2$

This study designed and synthesized the BPs-$FeSe_2$ nanosystem, which was featured with enhanced photothermal conversion efficiency and MRI-guided therapy. $FeSe_2$ was covalent on the surface of BPs to enable MRI-guided therapy. The BPs could then achieve photothermal conversion. The $FeSe_2$ nanoparticles were synthesized via the heat injection method. TEM was used to observe the morphology of BPs-$FeSe_2$. The uniform size of $FeSe_2$ in Fig. 1a is about 8 nm with good dispersion. The BPs with a size of about 200 nm were obtained through the classical liquid-phase exfoliation method [57] shown in Fig. 1b. The BPs dissolved in ethanol were injected into as-synthesized $FeSe_2$ nanoparticles and reacted overnight under N_2 atmosphere at room temperature. As shown in Fig. 1c, $FeSe_2$ nanoparticles were uniformly dispersed on BPs. Interestingly, we found that the thickness of BPs would affect the density of $FeSe_2$ decorated on the surface of BPs. BPs with various thicknesses were obtained under different ultrasound time. By adding BPs with a thickness of about 2.4 nm, the $FeSe_2$ nanoparticles were completely decorated on the surface (Additional file 1: Figure S1e, f). As the thickness of BPs increased, the density of $FeSe_2$ nanoparticles decorated on the BPs was reduced (Additional file 1: Figure S1a–d). We speculated that the thinner the BPs, the more lone pair electrons are exposed, leading to the easier covalent binding to $FeSe_2$. Meanwhile, by changing the amount of added $FeSe_2$, the density of $FeSe_2$ modified on the surface of BPs could also be adjusted (Additional file 1: Figure S2). When the $FeSe_2$: BPs ratio was 1:1, only a small part of $FeSe_2$ was modified on the surface of BPs. With the increase of $FeSe_2$ addition, the density of $FeSe_2$ nanoparticles on the BPs increased. Notably, when $FeSe_2$ was added at the $FeSe_2$: BPs ratio of 4:1, $FeSe_2$ nanoparticles were completely modified on the surface of BPs. However, if an excess of $FeSe_2$ was added (at the $FeSe_2$: BPs ratio of 5:1), a small part of the $FeSe_2$ was scattered around the BPs. Finally, we chose the thickness of BPs about 2 nm and the feeding $FeSe_2$: BPs ratio of 4:1 to prepare BPs-$FeSe_2$ for subsequent experiments. The interplanar spacing of 0.339 nm and 0.305 nm of high-resolution TEM (HR-TEM) in Fig. 1d, e; were matched with the (0 2 1) plane of P and the (1 1 1) plane of $FeSe_2$, respectively. The distribution of Fe, Se and P elements in the BPs-$FeSe_2$ nanosheet was observed in EDS data, which confirmed that BPs-$FeSe_2$ were successfully established (Fig. 1f). As shown in Fig. 1g, h, the atomic force microscopy (AFM) image revealed the morphology of the BPs-$FeSe_2$, and the height measured was about 10 nm, where the thickness of BPs was about 2 nm (Fig. 1i) and the height of $FeSe_2$ was about 8 nm. As shown in Fig. 1j, compared with the absorption spectra of $FeSe_2$, the significant representative absorption profiles in the NIR region are fully retained in BPs-$FeSe_2$ due to the intrinsic absorption characteristics of BPs, providing rationale for photothermal mechanism. The UV–vis absorption spectra in Additional file 1: Figure S3 exbibited that BPs-$FeSe_2$ showed strong optical absorption from NIR-I to NIR-II window, suggesting that the BPs-$FeSe_2$ heteronanostructure was a potential candidate for application in NIR-II PTA. Raman scattering

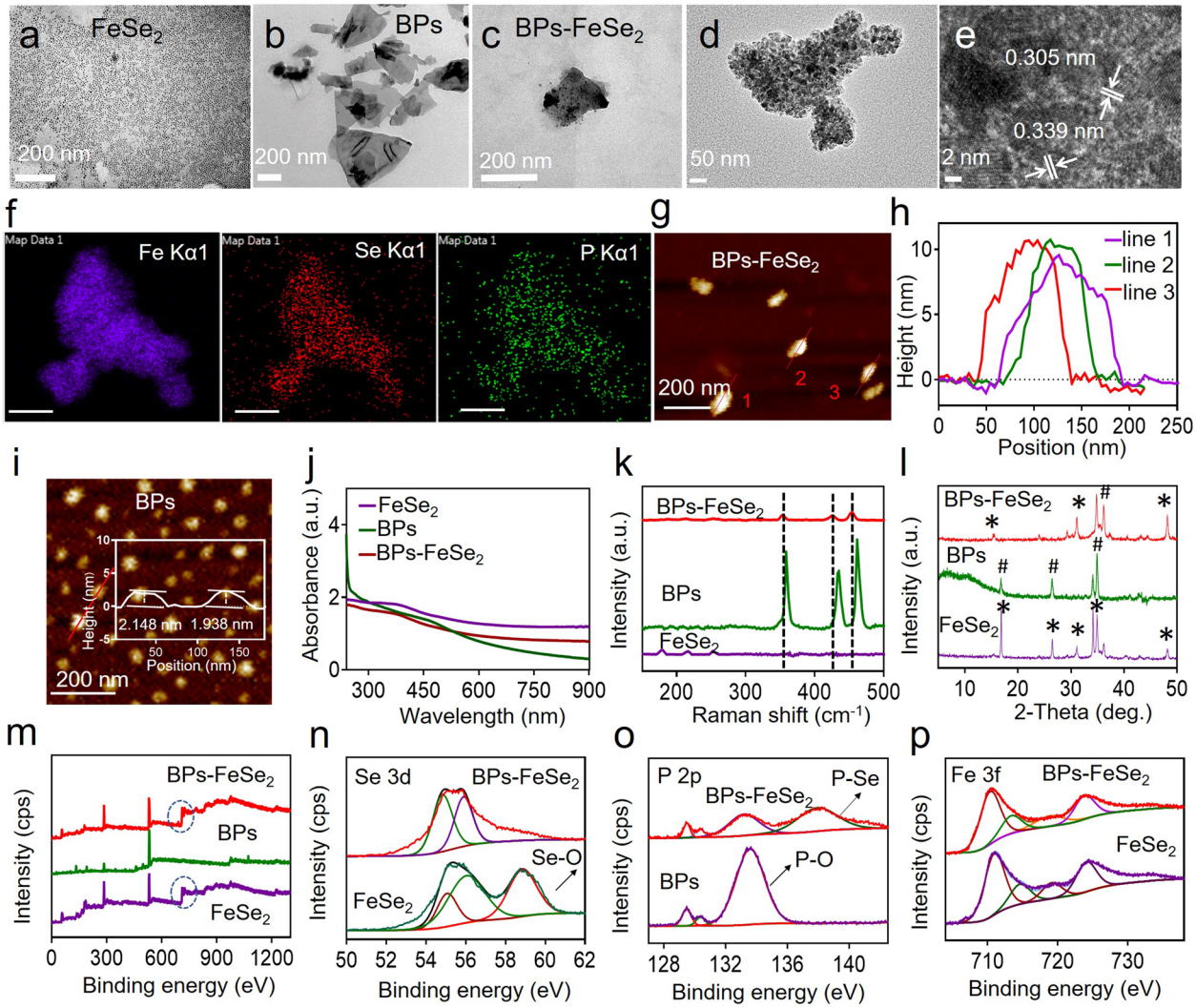

Fig. 1 Characterization of BPs-$FeSe_2$. TEM image of **a** $FeSe_2$; **b** BPs; and **c** BPs-$FeSe_2$. **d** HR-TEM images of BPs-$FeSe_2$. **e** Lattice fringes of **d**. **f** EDS elemental mapping images of BPs-$FeSe_2$ (scale bar = 50 nm). **g** AFM image of BPs-$FeSe_2$. **h** Height profiles along the red lines in **g**. **i** AFM image of BPs. **j** UV–vis absorption spectra of $FeSe_2$, BPs and BPs-$FeSe_2$. **k** Raman spectra of $FeSe_2$, BPs and BPs-$FeSe_2$. **l** XRD spectra of $FeSe_2$, BPs and BPs-$FeSe_2$. **m**–**p** XPS spectra of P 2p, Se 3d and Fe 2p compared with $FeSe_2$, BPs or BPs-$FeSe_2$

was further introduced to characterize the $FeSe_2$, BPs and BPs-$FeSe_2$ as in Fig. 1k. BPs-$FeSe_2$ showed three representative Raman peaks at 358.4, 434.8 and 433.1 cm^{-1} ascribed to A_g^1, B_{2g} and A_g^2 of BPs, respectively, confirming the introduction of $FeSe_2$ on the BPs. The structure of the nanoparticles was studied by X-ray diffraction (XRD). As shown in Fig. 1l, the representative diffraction peaks of BPs-$FeSe_2$ were matched with $FeSe_2$ and BPs, revealing the co-existence of $FeSe_2$ and BPs. X-ray photoelectron spectroscopy (XPS) was used to detect the chemical composition and binding energies of $FeSe_2$, BPs and BPs-$FeSe_2$, respectively. As shown in Fig. 1m, full-spectrum comparison confirmed the existence of $FeSe_2$ on BPs. It should be noted that there is a peak of 58.91 eV in the Se 3d high-energy region of $FeSe_2$, referring to Se-O, indicating that the individual $FeSe_2$ is oxidized, while the absence of analogous peaks in the BPs-$FeSe_2$ Se 3d spectrum indicates that the oxidation of $FeSe_2$ in BPs-$FeSe_2$ is negligible in Fig. 1n. As shown in Fig. 1o, the peak of P 2p at 133.9 eV was attributed to P-O, which indicated that both BPs and BPs-$FeSe_2$ were oxidized, but the oxidation degree of BPs-$FeSe_2$ was remarkably weaker than that of bare BPs. Besides, the characteristic peak of BPs-$FeSe_2$ in 138.25 eV represented the P-Se bond, while P alone did not appear. As shown in Fig. 1p, the two strong peaks at 724.68 and 710.87 eV are associated with Fe $2p_{1/2}$ and Fe

$2p_{3/2}$, confirming the formation of $FeSe_2$. These results revealed that the covalent P-Se bond between $FeSe_2$ and BPs could reduce the oxidation of BPs and $FeSe_2$. According to previous reports, BPs are sensitive to water and oxygen, and $FeSe_2$ contains Fe^{2+}, so they are easily oxidized. Owing to the covalent P-Se bond, the oxidation degree of $FeSe_2$ is weakened, and the lone pair electrons on the surface of black phosphorus are occupied, which reduces the exposure of lone pair electrons in air to prevent the oxidation, leading to excellent stability of BPs-$FeSe_2$-PEG. Taken together, the BPs-$FeSe_2$ was successfully synthesized based on the above results.

Stability and photothermal performance of BPs-$FeSe_2$-PEG

To further improve the biomedical application of the as-synthesized BPs-$FeSe_2$, mNH_2-PEG was used to coat it to enhance its water solubility and bioavailability (Additional file 1: Figure S4). Then the water-soluble PEGylated $FeSe_2$, BPs and BPs-$FeSe_2$ were obtained. To evaluate the influence of $FeSe_2$ on the stability of BPs, the PEGylated $FeSe_2$, BPs and BPs-$FeSe_2$ were dispersed in ultrapure water for 5 days. The corresponding absorption spectra were shown in Fig. 2a–c. In the ultraviolet and near-infrared regions, PEGylated $FeSe_2$, BPs and BPs-$FeSe_2$ showed typical broad absorption bands. Nevertheless, the absorbance intensity of BPs-$FeSe_2$-PEG only showed a negligible change, while that of $FeSe_2$-PEG and BPs-PEG decreased remarkably with time. Interestingly, BPs-$FeSe_2$-PEG still showed good

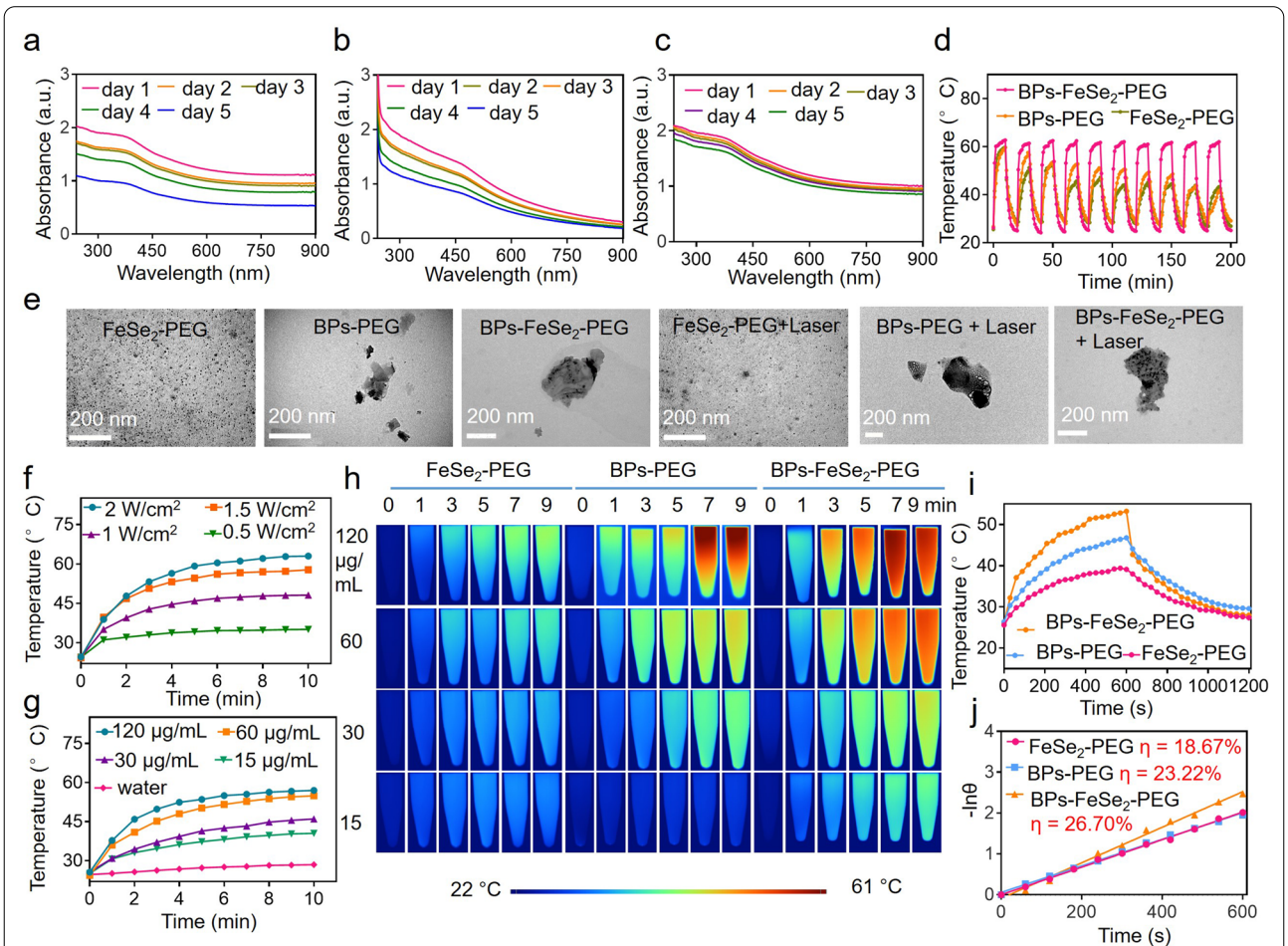

Fig. 2 Stability of BPs-$FeSe_2$-PEG. **a**–**c** UV–vis absorption spectra of PEGylated $FeSe_2$, BPs and BPs-$FeSe_2$ solutions for 5 days. **d** Photostability of PEGylated $FeSe_2$, BPs and BPs-$FeSe_2$ under NIR laser irradiation for 10 cycles (120 μg/mL, 1.5 W/cm^2, 10 min). **e** TEM images of PEGylated $FeSe_2$, BPs and BPs-$FeSe_2$ after 10 cyclic irradiation. **f** Temperature curves of BPs-$FeSe_2$-PEG solution (120 μg/mL, 10 min) under the irradiation of NIR laser various power (0.5, 1, 1.5, 2 W/cm^2). **g** Temperature curves of BPs-$FeSe_2$-PEG solution at different concentration (0, 15, 30, 60, 120 μg/mL) with NIR laser irradiation (1.5 W/cm^2, 10 min). **h** Infrared thermal image. **i** The temperature increment curve and the cooling curve of PEGylated $FeSe_2$, BPs and BPs-$FeSe_2$. **j** Line curve of − lnθ vs time obtained from the cooling period of **i**

stability on the 14th day (Additional file 1: Figure S5), while the BPs alone was almost completely degraded. The decrease in the absorbance of BPs may be attributed to the existence of lone pair electrons on the surface. As a result, when BPs were exposed to air, they were easily oxidized to PxOy. Besides, the phosphoric acid was formed when BPs were exposed to aqueous media. Both reasons eventually lead to the degradation of BPs. Photothermal stability is one of the significant factors to be envisioned as photothermal reagents. Consequently, we investigated the photothermal stability of PEGylated $FeSe_2$, BPs and BPs-$FeSe_2$ in water under NIR laser irradiation. PEGylated $FeSe_2$, BPs and BPs-$FeSe_2$ aqueous solutions were exposed to NIR laser to monitor the temperature change (laser on). Then, the solutions were cooled to room temperature (laser off). Interestingly, the photothermal effect of BPs-$FeSe_2$-PEG showed no noticeable decrease during 10 cycles under irradiation for 200 min. By contrast, the photothermal effect of $FeSe_2$-PEG and BPs-PEG decreased significantly in the same condition (Fig. 2d), which indicated the excellent thermal stability of BPs-$FeSe_2$-PEG. Besides, the TEM images in Fig. 2e revealed the morphology of BPs-$FeSe_2$-PEG, a negligible change after irradiation, indicating its high photostability. Then the stability of BPs-$FeSe_2$-PEG in different simulating intracellular environments was investigated, and the morphological changes were observed. As shown in Additional file 1: Figure S6, the morphology was obviously dissociated after treatment with pH at 5.3 and lysozyme, while BPs-$FeSe_2$-PEG in pH at 7.4 and 6.8 showed no significant change. Moreover, the BPs-$FeSe_2$-PEG markedly dissociated in the condition of EJ bladder cell lysate. The above results collectively revealed that BPs-$FeSe_2$-PEG possessed excellent water stability in simulated normal biological systems and degradability in simulated tumor systems, which endowed BPs-$FeSe_2$-PEG great potential as a photothermal agent. Considering the great potential as a photothermal agent, the photothermal performance of BPs-$FeSe_2$-PEG was investigated by exposing various concentrations of BPs-$FeSe_2$-PEG to NIR laser. The temperature change was recorded at intervals using an IR thermal driver. As shown in Fig. 2f–h and Additional file 1: Figure S7a–d, those photothermal curves disclosed concentration and power-dependent heating effects and reached equilibrium within 5 min. When the BPs-$FeSe_2$-PEG solution was exposed to laser at a density of 1.5 W/cm^2 for 10 min, the temperature swiftly rose to 57 °C, which could ablate the tumor. Nevertheless, only 4 °C of increased temperature was detected in water, indicating the good photothermal effect of BPs-$FeSe_2$-PEG. Besides, the photothermal conversion efficiency (η) of PEGylated $FeSe_2$, BPs and BPs-$FeSe_2$ were calculated referring to previous methods (Fig. 2i, j). The value of BPs-$FeSe_2$-PEG was 26.7%, which was higher than that of $FeSe_2$-PEG (18.67%), BPs-PEG (23.22%) and other classical inorganic photothermal reagent [58–60].

Photothermal mechanism of BPs-$FeSe_2$ heteronanostructure

To understand the mechanism of the enhanced photothermal performance of BPs-$FeSe_2$ heteronanostructure, the physical properties of $FeSe_2$ and BPs were investigated. As shown in Fig. 3b, c, the valance band (VB) values of $FeSe_2$ and BPs were identified by XPS spectra and calculated to be about 0.85 eV and 0.46 eV, respectively. The band gaps (Eg) of $FeSe_2$ and BPs obtained from UV–vis-NIR diffuse spectra were about 1.84 eV and 1.78 eV, respectively (Fig. 3d, e). Electrochemical impedance spectroscopy (EIS) revealed the smallest diameter of BPs-$FeSe_2$, suggesting that BPs-$FeSe_2$ heteronanostructure had the lowest impedance and electron–hole recombination rate (Fig. 3f). The photocurrent responses were detected under irradiation, which provided evidence of efficient separation and transmission of photoinduced charges. As shown in Fig. 3g, a photocurrent had a response when turning on the light, but no response was observed when the light was off, confirming the efficient charge separation and transmission. Moreover, BPs-$FeSe_2$ had the highest photocurrent response, indicating the fast separation of electron–hole pairs and low rate of electron–hole pairs recombination between $FeSe_2$ and BPs. To illustrate the transferring mechanism of electron–hole pairs, the types of active radicals generated by BPs-$FeSe_2$ under irradiation were detected by electron spin resonance (ESR). As shown in Fig. 3h, i, BPs-$FeSe_2$ under irradiation for 5 min showed the most strong $^1O_2$ signal than other groups, which indicated the generation of $^1O_2$ radical. The possible mechanism of $FeSe_2$ heteronanostructures enhanced photothermal performance was proposed. The energy band and electron transfer were vividly illustrated in Fig. 3a. The valence electrons (VB) of $FeSe_2$ and BPs were excited into the conduction band (CB) of $FeSe_2$ and BPs after irradiation, which caused the generation of electron–hole pairs. The photoinduced electrons transferred from the CB of BPs to the CB of $FeSe_2$, while the holes transferred from the VB of $FeSe_2$ to the VB of BPs, indicating the effective separation of photoinduced electrons and holes. The low recombination rate means an enhanced lifetime of photogenerated carriers, leading to more photogenerated carriers generating $^1O_2$. Besides, under irradiation, the photogenerated carriers could be changed into hot carriers and then produce phonons to release excess energy to return to equilibrium state via

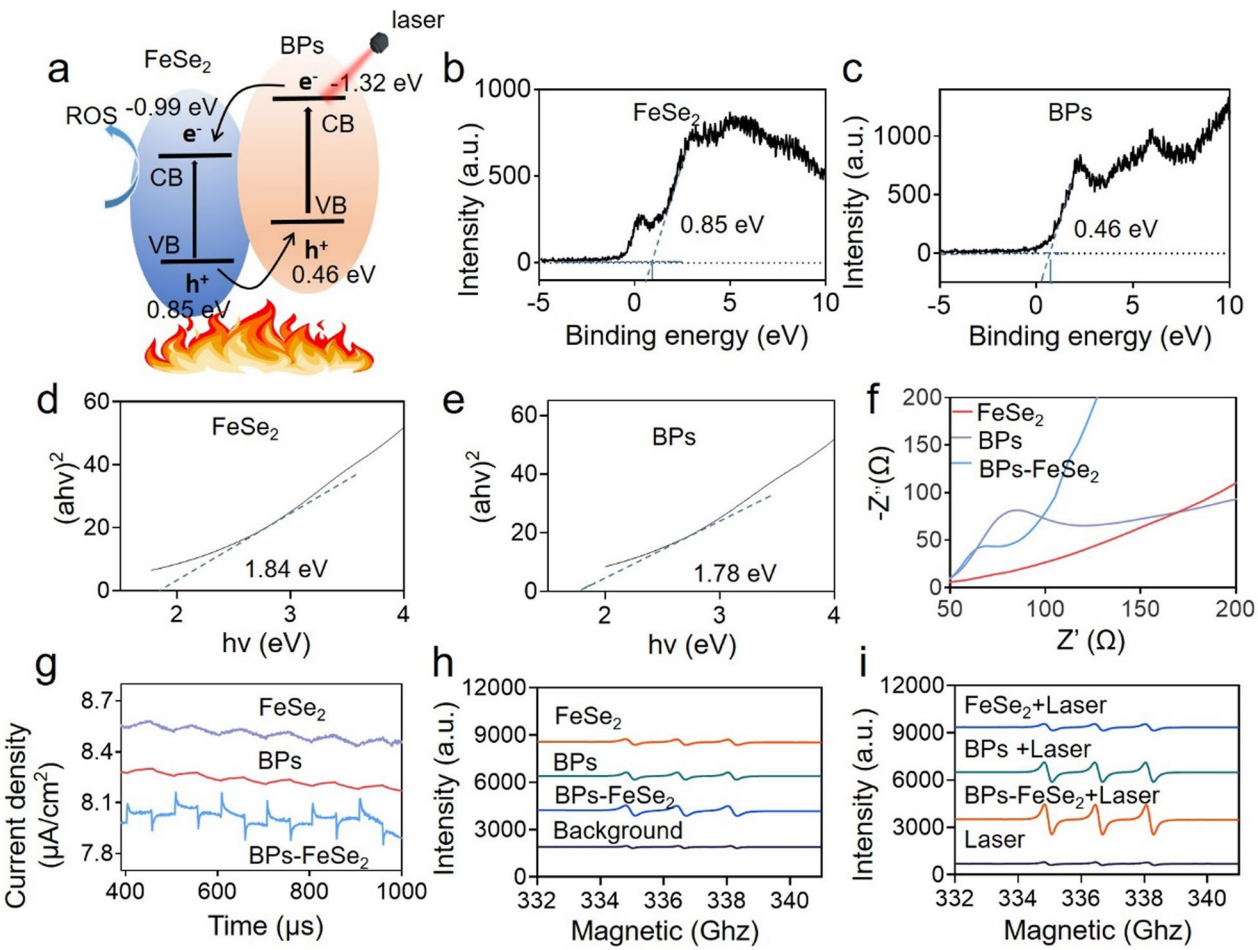

Fig. 3 Photothermal mechanism of BPs-$FeSe_2$. **a** Photothermal mechanism of the charge transfer of BPs-$FeSe_2$ under light irradiation. **b**, **c** The valance band of $FeSe_2$ and BPs. **d**, **e** The bandgap of $FeSe_2$ and BPs is calculated by KubelkaMunk equation. **f** EIS spectra of $FeSe_2$, BPs and BPs-$FeSe_2$. **g** Photocurrent with $FeSe_2$ and BPs responded to the on/off light irradiation. **h**, **i** ESR spectra of $FeSe_2$, BPs and BPs-$FeSe_2$ without/with NIR laser for $^1O_2$ (100 μg/mL, 1.5 W/cm^2, 5 min)

non-radiative recombination at the interface of $FeSe_2$ and BPs. The excess energy caused enhanced photothermal performance of BPs-$FeSe_2$ than that of single $FeSe_2$ or BPs. In summary, the radiative recombination of the holes and electrons was effectively inhabited and the lifetime of the holes and electrons was increased in the BPs-$FeSe_2$ heterostructure, which resulted in a high degree of photothermal conversion. A lot of researches have demonstrated that the heterostructure could enhance the effective separation of photoinduced electrons and holes, delay the recombination of electron–hole pairs, and increase the ROS yield during the electron–hole pair transfer under laser irradiation. For instance, Wu et al. proved that a heterojunction which was composed of a photoresponsive metal–organic framework and Prussian blue could exhibit an enhanced photothermal effect [61]. Hence, we infer that, in general, a heterostructure, which could enhance the effective separation of photoinduced electrons and holes and delay the recombination of electron–hole pairs under laser irradiation, can lead to the improvement of photothermal efficiency of this heterostructure.

Anticancer efficacy of BPs-$FeSe_2$-PEG in vitro

It is worth examining the temperature variation of BPs-$FeSe_2$-PEG at the cellular level under NIR laser irradiation. Bladder cancer tumor cells (EJ cells) were used as models to analyze the effects of photothermal therapy on nanoparticles at the cellular level. As shown in Fig. 4a, b and Additional file 1: Figure S8a, b; the temperature rising rate was concentration-dependent and power-dependent. These results showed that at the same concentration (50 μg/mL), the temperature increased by 18 °C at a laser density of 1.5 W/cm^2, which was similar

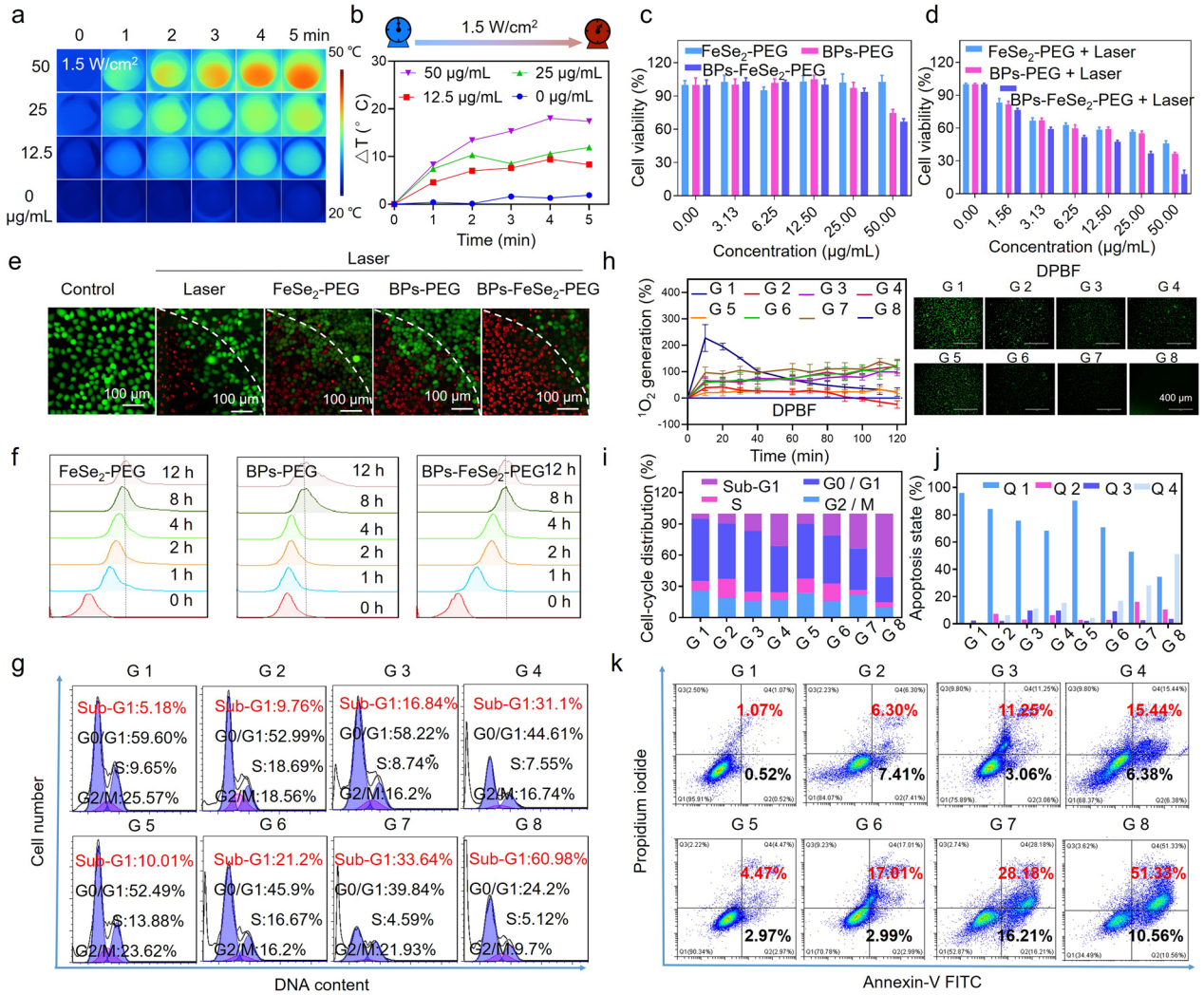

Fig. 4 Anticancer efficacy of BPs-$FeSe_2$-PEG in vitro. **a** Infrared thermal images and **b** temperature change of EJ cells incubated with different concentrations BPs-$FeSe_2$-PEG under NIR laser (1.5 W/cm^2, 5 min). **c**, **d** The EJ bladder cell viability of PEGylated $FeSe_2$, BPs and BPs-$FeSe_2$ at various concentrations with/without NIR laser for 72 h. (1.5 W/cm^2, 5 min). **e** Fluorescence images of EJ cells stained with calcein-AM (green) and PI (red) under different treatment (25 μg/mL, 1.5 W/cm^2, 5 min). **f** Cellular uptake analysis results of the same concentration of coumarin-6 labeled PEGylated $FeSe_2$, BPs and BPs-$FeSe_2$ in EJ cells by flow cytometry analysis (25 μg/mL). **g** Cell cycle arrest in EJ cells induced the same concentration of PEGylated $FeSe_2$, BPs and BPs-$FeSe_2$ with/without NIR laser (25 μg/mL, 1.5 W/cm^2, 5 min). G 1: Control; G 2: $FeSe_2$-PEG; G 3: BPs-PEG; G 4: BPs-$FeSe_2$-PEG; G 5: laser; G 6: $FeSe_2$-PEG + laser; G 7: BPs-PEG + laser; G 8: BPs-$FeSe_2$-PEG + laser. **h** The generation of singlet oxygen during 120 min and representative fluorescence photos at 120 min in EJ bladder cells under different treatment (100 μg/mL, 1.5 W/cm^2, 1 min). **i** Histogram of cell cycle phase of EJ bladder cells under different treatments matched with **g**. **j** Histogram of apoptosis of EJ bladder cells detected by AnnexinV/PI Staining matched with **k**. **k** Annexin V-FITC/PI double staining results under different treatment (25 μg/mL, 1.5 W/cm^2, 5 min)

to that of 2 W/cm^2, but only 7.5 °C at the laser density of 1 W/cm^2. Therefore, 1.5 W/cm^2 was determined as a suitable laser density for subsequent experiments. Overall, the results revealed that BPs-$FeSe_2$-PEG has excellent potential as a photothermal reagent. Then, in vitro phototherapeutic effects of BPs-$FeSe_2$-PEG against EJ bladder cells were evaluated by 3-(4, 5-dimethylthiazol-2-yl)-2, 5-diphenyltetrazolium bromide (MTT) assay. As shown in Fig. 4c, d, after NIR laser irradiation, 63.16% of the BPs-$FeSe_2$-PEG (25 μg/mL) treated cells were killed, which was higher than those treated with $FeSe_2$-PEG (41.64% cell death) and BPs-PEG (44.89% cell death). The therapeutic efficacy of BPs-$FeSe_2$-PEG showed a dose-dependent manner.

Besides, the effect of the nanoparticle on SVHUC-1 cells was studied. As shown in Additional file 1: Figure S9, the BPs-$FeSe_2$-PEG exhibited a high degree of safety to normal cells. To visually disclose the anticancer activities

of PEGylated $FeSe_2$, BPs and BPs-$FeSe_2$ combined with PTT, calcein AM and PI co-staining was performed. As shown in Fig. 4e, in the area of laser irradiation illumination, the cell death was induced by PEGylated $FeSe_2$, BPs and BPs-$FeSe_2$. The clear dividing line could be observed between dead (red) and live (green) cells. The cells treated with BPs-$FeSe_2$-PEG showed the most significant tendency to die, attributed to the great photothermal conversion efficiency, leading to the highest temperature among them. In contrast, cells only treated with NIR laser had slight cell death, revealing higher anticancer efficacy of BPs-$FeSe_2$-PEG. Then we utilized flow cytometry to study the intracellular uptake of coumarin-6 labeled PEGylated $FeSe_2$, BPs and BPs-$FeSe_2$ in EJ bladder cells at different times. The cellular uptake of PEGylated $FeSe_2$, BPs and BPs-$FeSe_2$ was time-dependent and reached saturation within 8 h (Fig. 4f). Furthermore, to vividly observe the intracellular localization of coumarin-6-labeled BPs-$FeSe_2$-PEG in EJ cells, the nucleus and lysosomes were stained using lysotracker (red) and DAPI (blue), respectively. As shown in Additional file 1: Figure S10, the cytoplasm of EJ cells obviously showed green fluorescence after 1 h. Moreover, the overlapping color of red and green fluorescence can be found after 8 h, which is consistent with cellular uptake. As a result, the BPs-$FeSe_2$-PEG enter EJ bladder cells through endocytosis, which was time-dependent. To study the biological effects of BPs-$FeSe_2$-PEG heteronanostructure combination with laser, flow cytometry was employed to investigate EJ bladder cells cycle distribution proportion. As shown in Fig. 4g, i, the sub-G 1 peak of laser alone group was 10.01%. However, it should be noted that the sub-G 1 peak of BPs-$FeSe_2$-PEG combination with laser group remarkably enhanced to 60.98%. Those results provided evidence that BPs-$FeSe_2$-PEG combined with laser-induced cell apoptosis inhibited the growth of EJ bladder cells. The flow cytometry studies illuminate that BPs-$FeSe_2$-PEG exhibits more phototherapeutic effects than $FeSe_2$-PEG and BPs-PEG, which could be ascribed to good stability and great photothermal conversion efficiency of BPs-$FeSe_2$-PEG. To further illustrate the antitumor mechanisms of BPs-$FeSe_2$-PEG, we used Annexin V-FITC / PI double labeling kit to analyze EJ cell apoptosis with/without laser irradiation. As shown in Fig. 4j, k, BPs-$FeSe_2$-PEG mainly enhanced cell apoptosis in the late-stage. Reactive oxygen species (ROS) include superoxide anions ($^{-}O_2$), hydroxyl radical (OH), hydrogen peroxides (H_2O_2) and singlet oxygen ($^1O_2$). The overproduction of ROS leads to cell apoptosis [62]. The production of hydrogen peroxide and singlet oxygen induced by cotreatment was analyzed by 2, 7-dichlorodihydrofluorescein diacetate (DCFH-DA) and 1, 3-diphenylisobenzofuran (DPBF) probes, respectively. The combination treatments enhanced the level of H_2O_2 in EJ cells shown in Additional file 1: Figure S11. Besides, as shown in Fig. 4h, the intracellular $^1O_2$ level induced by BPs-$FeSe_2$-PEG combination with laser increased remarkably in 40 min than that of other treatment groups. The fluorescence images were consistent with the experimental results. The results indicated that the combination of laser and BPs-$FeSe_2$-PEG elevated the generation of $^1O_2$ and H_2O_2, which caused the tumor apoptosis.

Imaging-guided therapy in vivo

MRI provides abundant tumor information for pretreatment diagnosis. It provides a basis for real-time monitoring of therapeutic progression, judging the curative effect, and realizing the precise treatment of cancer. $FeSe_2$ illustrated the superparamagnetic nature as previously reported. The $FeSe_2$ core could react with H_2O and needed to be coated with PEG to dissolve in aqueous solution. Then we evaluated different concentrations (Fe concentration 0, 0.00125, 0.0025, 0.005, 0.01, 0.02 mM) of $FeSe_2$-PEG and BPs-$FeSe_2$-PEG applied for MRI analysis in vitro. T_2-weighted MRI images revealed the dose-dependent property of those NPs (Fig. 5a). The transverse relaxivity (r_2) of $FeSe_2$-PEG or BPs-$FeSe_2$-PEG was calculated to be 211.65 mM^{-1} s^{-1} or 402.06 mM^{-1} s^{-1}, respectively (Fig. 5b). It has been reported that the size, concentration, aggregation and magnetization of contrast agents could affect their performances [63–69]. When the total amount of $FeSe_2$ was constant, the clustering of the $FeSe_2$ core and the chemical composition of the coating determined enhanced T_2-weighted imaging ability of BPs-$FeSe_2$-PEG. The mPEG-NH_2 coating of BPs-$FeSe_2$-PEG could form hydrogen bonds with water around the material to immobilize water molecules, which affected the nuclear relaxation. The density of $FeSe_2$ on BPs was larger than $FeSe_2$ alone, which was equivalent to the aggregation of the $FeSe_2$ core. The aggregation of magnetic grains could enhance the T_2 relaxivity of BPs-$FeSe_2$-PEG. This indicated that BPs-$FeSe_2$-PEG was a promising T_2 MRI contrast agent. To observe the in vivo MR imaging effect of the nanoparticle more accurately, mice bearing EJ bladder tumors were injected with $FeSe_2$-PEG and BPs-$FeSe_2$-PEG to monitor the accumulation of NPs in the tumor region. The T_2-weighted MRI images of tumor areas were obtained. As shown in Fig. 5c, darkening effects were observed in the tumor regions after injection. The effect had been the darkest at 2 h post-injection and then been bright gradually. The intensity of MRI signals in the tumor region showed that the mouse with BPs-$FeSe_2$-PEG displayed weaker signal intensity in 24 h than that of $FeSe_2$-PEG. The values of T_2 of BPs-$FeSe_2$-PEG in the tumor region were lower than that of $FeSe_2$-PEG in Fig. 5d. The MRI signal then gradually increased after 2 h

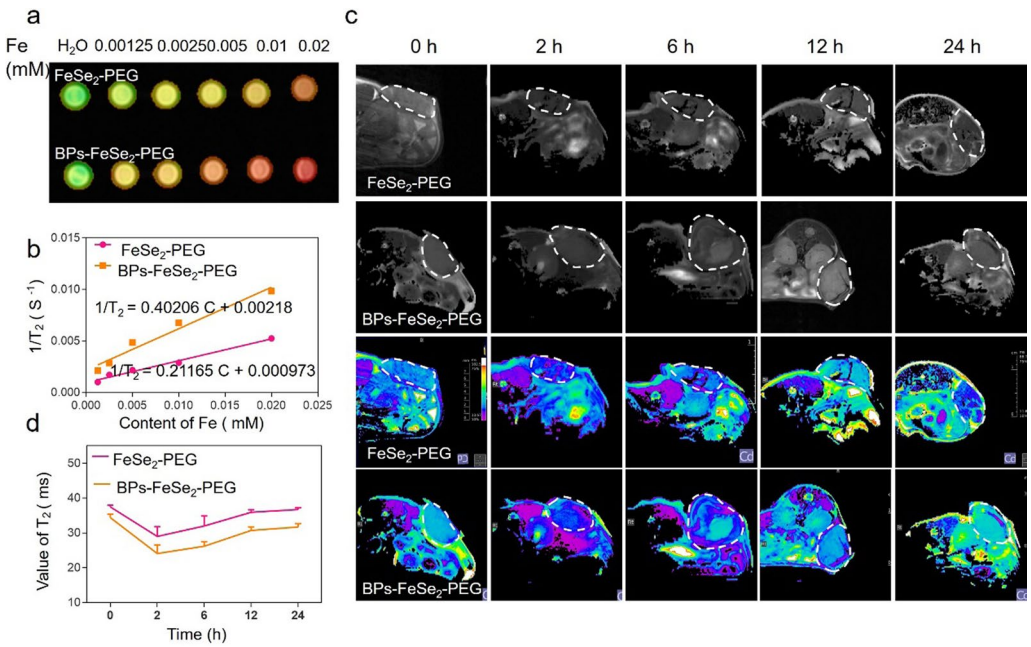

Fig. 5 Imaging analysis of BPs-$FeSe_2$-PEG. **a** T_2-MRI images of $FeSe_2$-PEG and BPs-$FeSe_2$-PEG solution at different concentrations (0–0.02 mM) in vitro. **b** T_2 relaxation rates of $FeSe_2$-PEG and BPs-$FeSe_2$-PEG solution under different concentrations. **c** T_2-weighted MRI images of mice bearing EJ bladder tumor after intravenous injection of $FeSe_2$-PEG and BPs-$FeSe_2$-PEG (10 mg/kg) for 0, 2, 6, 12 and 24 h. **d** The intensity of MRI signals matched with **c**

injection, suggesting clearance of the nanosheets from the cancer cells. As a result, the best time point for conducting photothermal therapy was at 2 h post-injection. These results suggested that the BPs-$FeSe_2$-PEG could be used to provide precise tumor-specific MRI guidance in tumor theranostics.

Photothermal therapy of BPs-$FeSe_2$-PEG in vivo

The antitumor efficacy of the BPs-$FeSe_2$-PEG in vivo is studied using EJ bladder tumor-bearing nude mice (Fig. 6a). PEGylated $FeSe_2$, BPs and BPs-$FeSe_2$ nanomaterials were administered via intravenous injection, and NIR laser was irradiated 1.5 W/cm^2 for 10 min at 2 h post-injection based on the MRI results. Mice were divided randomly into eight groups (n = 3), G 1: saline; G 2: $FeSe_2$-PEG; G 3: BPs-PEG; G 4: BPs-$FeSe_2$-PEG; G 5: laser; G 6: $FeSe_2$-PEG + Laser; G 7: BPs-PEG + Laser; G 8: BPs-$FeSe_2$-PEG + Laser. The temperature change of the tumor region with different nanoparticles during the PTT treatment was monitored by a thermal imager. As shown in Fig. 6b, c, the increase of temperature was time-dependent, and the temperature increased to 47.6, 50 and 61.2 °C after injected with $FeSe_2$-PEG, BPs-PEG, and BPs-$FeSe_2$-PEG, respectively. The tremendous therapeutic effect of BPs-$FeSe_2$-PEG upon laser compared with other groups after 21 days of treatment was clearly shown by the images of the tumor region in Fig. 6d. Some of the G 8 group tumors have even been ablated due to the combined effect of BPs-$FeSe_2$-PEG and NIR laser. Relative tumor volume and weight changes indicate that the combination of BPs-$FeSe_2$-PEG and NIR laser have excellent antitumor effects of inhibiting the growth of EJ bladder tumors (Fig. 6e, f). As shown in Fig. 6g, the bodyweight of all groups shows a stable trend for 21 days, revealing the negligible toxicity of nanoparticles. The changes of tumor volume in each group of mice within 21 days of treatment were recorded in Fig. 6h and Additional file 1: Figure S12. The H&E results of the tumor region further demonstrated that the group treated by the combination of BPs-$FeSe_2$-PEG and NIR laser promoted apoptosis of cancer cells in Fig. 6i. Tumor was further analyzed by Immunohistochemistry assay. The p53 plays an important role in inducing apoptosis in cells and regulating the progression of cell cycle [70]. The p53 signaling pathway was remarkably activated in G 8 group indicating the cell apoptosis increased. The G 8 group decreased the expression of Ki67, a marker for proliferation, indicating that tumor cell proliferation was inhibited. Moreover, to further analyze the antitumor efficacy of co-treatment, the apoptosis of tumor sections was detected by TUNEL staining assays. The green fluorescence intensity of G 6, G 7 and G 8 group were relatively higher than other groups, indicating larger numbers of cell apoptosis. The

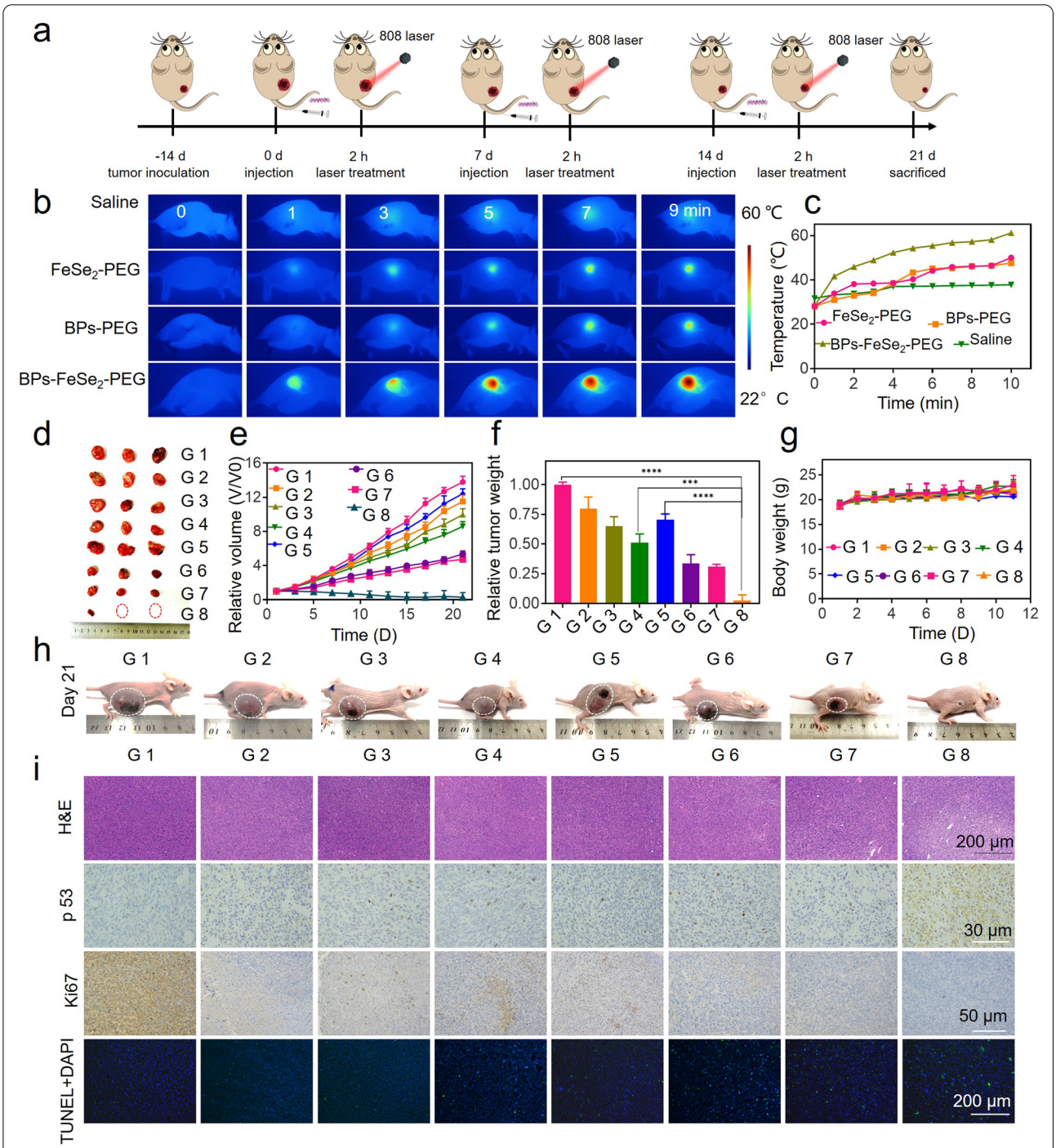

Fig. 6 Anticancer efficacy of BPs-$FeSe_2$-PEG in vivo. **a** Schematic illustration of BPs-$FeSe_2$-PEG (10 mg/kg) under NIR laser (1.5 W/cm^2, 10 min) to inhabit EJ bladder tumor growth. **b-c** Images and temperature of the tumor region injected with Saline, $FeSe_2$-PEG, BPs-PEG and BPs-$FeSe_2$-PEG under NIR laser. **d** Photos of tumors after 21 days of treatment. **e** Curves of relative tumor volume during 21 days. **f** Relative tumor weights after 21 days treatment; data are presented as mean ± SD (n = 3), (****P < 0.001, **P < 0.01, *P < 0.05*). **g** The body weight during 21 days treatment. **h** Photos of EJ bladder tumor-bearing mice with/without laser after 21 days. **i** H&E-stained; protein expression levels of p53 and Ki67 in tumor regions of different treatment groups by IHC assay, and TUNEL staining in the tumor region. G 1: saline, G 2: $FeSe_2$-PEG; G 3: BPs-PEG; G 4: BPs-$FeSe_2$-PEG; G 5: laser; G 6: $FeSe_2$-PEG + Laser; G 7: BPs-PEG + Laser; G 8: BPs-$FeSe_2$-PEG + Laser

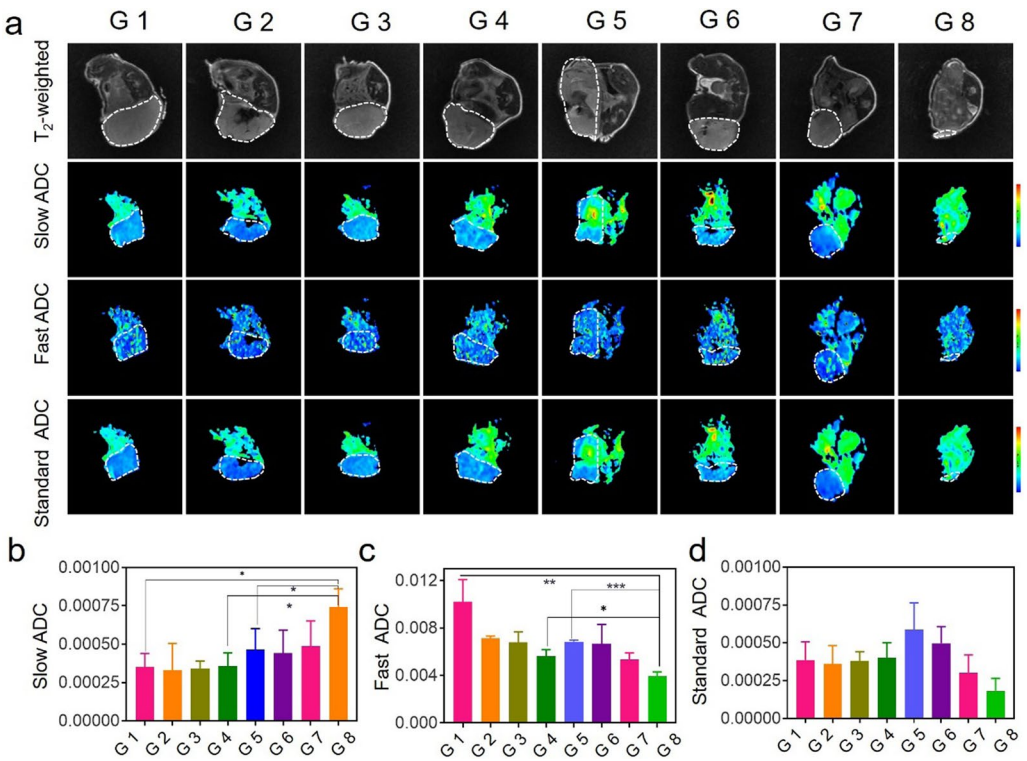

Fig. 7 T_2-weighted imaging analysis of tumor regions of different treatments after 21 days. **a** Images of T_2-weighted MRI, fast ADC, slow ADC and standard ADC of EJ bladder tumor model with different treatments at 21 days. **b** Values of slow ADC. **c** Value of fast ADC. **d** Value of standard ADC. G 1: saline, G 2: $FeSe_2$-PEG; G 3: BPs-PEG; G 4: BPs-$FeSe_2$-PEG; G 5: laser; G 6: $FeSe_2$-PEG + Laser; G 7: BPs-PEG + Laser; G 8: BPs-$FeSe_2$-PEG + Laser. Data are presented as means ± SD (n = 3), (****P < 0.001, **P < 0.01, or *P < 0.05)*

results demonstrated that BPs-$FeSe_2$-PEG heteronanostructure had an excellent inhibitory effect on EJ bladder tumors by improving cell apoptosis.

Evaluation of antitumor effects by MRI

The antitumor activity of BPs-$FeSe_2$-PEG was further evaluated by MRI. We obtained T_2-weighted MRI images of tumor areas of mice in different treatment groups after 21 days. BPs-$FeSe_2$-PEG cotreatment group presented the smallest tumor area than that of other groups after 21 days shown in Fig. 7a. Besides, the cell density and activity of tumor regions could be evaluated by slow ADC value. As shown in Fig. 7b, compared with the other groups, the enhanced slow ADC values in the tumor region of G 8 indicated a decrease in the density and activity of bladder tumor cells. Moreover, fast ADC signals are related to the blood flow in the tumor area in Fig. 7c. A weaker fast ADC intensity can be observed at the tumor region in the BPs-$FeSe_2$-PEG combined with the NIR laser treatment group. As shown in Fig. 7d, the value of standard ADC in G 8 decreases, demonstrating the excellent anticancer activity of BPs-$FeSe_2$-PEG. In summary, BPs-$FeSe_2$-PEG heteronanostructure combined with laser could significantly inhibit EJ bladder tumor growth in vivo.

Toxicity evaluation of BPs-$FeSe_2$-PEG in vivo

It is crucial to evaluate the safety of BPs-$FeSe_2$-PEG in vivo. All of the mice were sacrificed to collect their main organs and blood after 21 days of treatment. As shown in Fig. 8a, the main organs of H&E-stained results of the combined BPs-$FeSe_2$-PEG and laser exhibited no detectable toxicity to the major organs. Besides, as shown in Fig. 8b and Additional file 1: Figure S13, the biochemical indicator level of G 8 group of alanine aminotransferase (ALT), aspartate aminotransferase (AST), total protein (TP), globulin (GLOB), cholesterol (CHOL), uric acid (UA), Creatinine (CREA), urea (UREA), Glucose (GLU), high-density lipoprotein cholesterol (HDL-C), low-density lipoprotein cholesterol (LDL-C), triglyceride (TG), creatine kinase (CK), Lactate dehydrogenase (LDH) and albumin (ALB) showed no obviously difference compared with that of the healthy group.

The biodistribution of BPs-$FeSe_2$-PEG in the main organs and tumors of EJ bladder tumor mouse model

was evaluated to investigate the longer term biodistribution. The concentration of Se element after 21 days of treatment was measured by ICP-MS. As shown in Additional file 1: Figure S14, BPs-$FeSe_2$-PEG could accumulate in liver and tumor areas, suggesting that the liver was the main target organ and the BPs-$FeSe_2$-PEG could accumulate in tumor region for MRI-guided PTT. Besides, the results demonstrated that BPs-$FeSe_2$-PEG could be degraded and excreted over time and the BPs-$FeSe_2$-PEG was safe and had no accumulative toxicity. Besides, the pharmacokinetics of BPs-$FeSe_2$-PEG in vivo was studied. Then we used ICP-MS to measure the Se concentration in the blood of mice injected with 4 mg/kg BPs-$FeSe_2$-PEG [71]. The blood was obtained at 0.5, 1, 2, 4, 8, 12, 24, 48 and 72 h after injection. As shown in Additional file 1: Figure S15 and Table S1, the plasma Se concentration in blood sharply decreased and decayed to half in 17 h, suggesting that the nanoparticle was degraded and excreted over time. These results exhibit that the BPs-$FeSe_2$-PEG has good degradability in vivo.

The liver is the metabolic organ. Nanoparticles could penetrate the cell membrane into cells, through lipid peroxidation or promote the production of reactive oxygen species and other ways to cause liver injury, affecting the normal physiological function of the liver. The effects of BPs-$FeSe_2$-PEG heterodimer on liver inflammation and apoptosis in mice were evaluated by analyzing the expression of NF-Kβ and caspase-3. The NF-kβ receptor is a cytoplasmic protein complex responsible for regulating the expression of a variety of inflammatory mediators. Caspase-3 is considered as the central regulator of apoptosis, and the activated caspase-3 signal pathway induces apoptosis of tumor cells. It should be noted that the expression of NF-Kβ and caspase-3 in the liver of all groups of mice was negative in Fig. 8c. These results indicate the BPs-$FeSe_2$-PEG heteronanostructure does not cause liver inflammation and apoptosis and has no obvious hepatotoxicity. In summary, BPs-$FeSe_2$-PEG is an effective and safe nanoparticle to inhibit the growth of EJ bladder tumors.

Conclusions

In summary, we have designed a BP-based heteronanostructure nanoparticle system and demonstrated its enhanced photothermal conversion efficiency mechanism, good photostability, MRI property and excellent antitumor effects. The mechanism reveals that BPs-$FeSe_2$-PEG heteronanostructure could enhance separation of photoinduced electron–hole pairs, accelerate charge transfer and reduce the recombination rate of photoinduced carriers, resulting in the generation of phonons to release excess energy to return to equilibrium state via non-radiative recombination at the interface of $FeSe_2$ and BPs, thus leading to higher photothermal conversion than free $FeSe_2$ and BPs. The presence of Fe enables BPs-$FeSe_2$-PEG to be used as an MRI agent for imaging-directed photothermal treatment. The aggregation of $FeSe_2$ on the surface of BPs and the formation of hydrogen bonds could enhance the T_2 relaxivity of BPs-$FeSe_2$-PEG. Besides, MRI in tumor help to choose the best time point for photothermal therapy. Finally, BPs-$FeSe_2$-PEG heteronanostructure shows remarkable photoablation of tumors and has no obvious toxicity to major organs. In summary, this work provides a novel strategy for fabricating BPs-based heteronanostructure nanomaterials that can simultaneously enhance photothermal conversion efficiency and photostability and realize MRI for precise cancer therapeutic efficacy. Our strategy paves a new path to design black phosphorus-based heterostructures for biomedical applications, integrated diagnosis and therapy.

(See figure on next page.)

Fig. 8 Toxicity evaluation of BPs-$FeSe_2$-PEG in vivo. **a** H&E staining of main organs of the mice under different treatments for 21 days. **b** ALT; AST; TP; ALB; cREA; UA; CHOL; LDL-C and HDL-C in all groups of mice with different treatments for 21 days (n = 3). **c** Hepatic NF-kβ expression and caspase-3 expression of different groups of mice by IHC assay. G 1: saline, G 2: $FeSe_2$-PEG; G 3: BPs-PEG; G 4: BPs-$FeSe_2$-PEG; G 5: laser; G 6: $FeSe_2$-PEG + Laser; G 7: BPs-PEG + Laser; G 8: BPs-$FeSe_2$-PEG + Laser

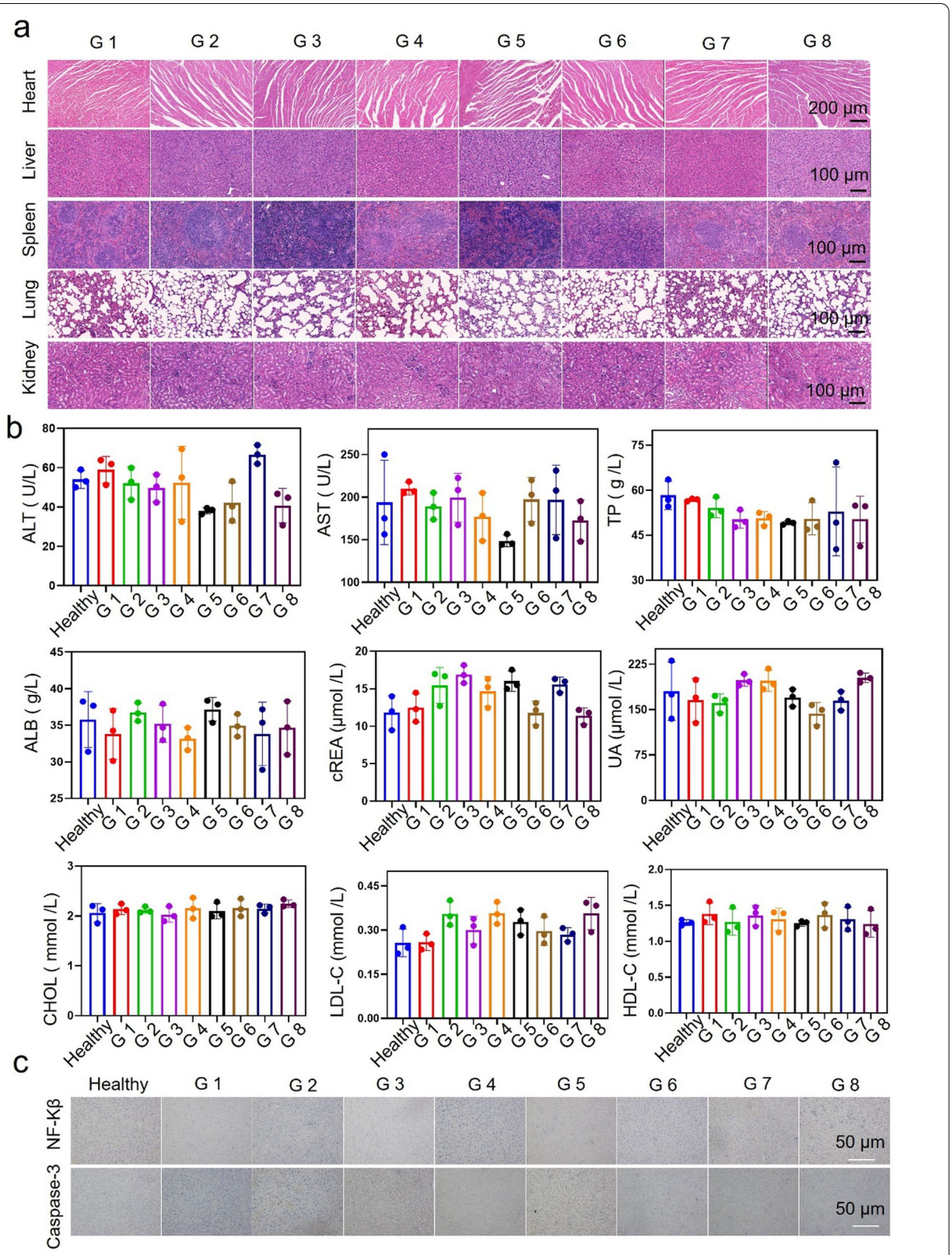

Fig. 8 (See legend on previous page.)

Abbreviations
$FeSe_2$: Ferrous selenide; BPs: Black phosphorus nanosheets; mPEG-NH_2: Methoxy poly (ethylene glycol); XRD: X-ray powder diffraction; XPS: X-ray photoelectron spectroscopy; TEM: Transmission electron microscopy; HR-TEM: High-resolution TEM; AFM: Atomic force microscope; EDS: Energy-dispersive X-ray spectroscopy; η: Photothermal conversion efficiency; MTT: 3-(4, 5-Dimethylthiazol-2-yl)-2, 5-diphenyltetrazolium bromide; DCFH-DA: 2, 7-Dichlorodihydrofluorescein diacetate; DPBF: 1, 3-Diphenylisobenzofuran; ROS: Reactive oxygen species; $^{-}O_2$: Superoxide anions; .OH: Hydroxyl radical; H_2O_2: Hydrogen peroxides; $^1O_2$: Singlet oxygen; r_2: Transverse relaxivity; ALT: Alanine aminotransferase; AST: Aspartate aminotransferase; TP: Total protein; GLOB: Globulin; CHOL: Cholesterol; UA: Uric acid; CREA: Creatinine; UREA: Urea; GLU: Glucose; HDL-C: High-density lipoprotein cholesterol; LDL-C: Low-density lipoprotein cholesterol; TG: Triglyceride; CK: Creatine kinase; LDH: Lactate dehydrogenase; ALB: Albumin; G 1: Saline; G 2: $FeSe_2$-PEG; G 3: BPs-PEG; G 4: BPs-$FeSe_2$-PEG; G 5: Laser; G 6: $FeSe_2$-PEG + Laser; G 7: BPs-PEG + Laser; G 8: BPs-$FeSe_2$-PEG + Laser; ICP-MS: Inductively coupled plasma mass spectrometry.

Supplementary Information

The online version contains supplementary material available at https://doi.org/10.1186/s12951-021-00905-5.

Additional file 1: Figure S1. AFM and TEM images of BPs and BPs-$FeSe_2$ with different thicknesses. **Figure S2.** TEM images of BPs-$FeSe_2$ nanostructures prepared with various $FeSe_2$: BPs feeding ratios. **Figure S3.** UV–vis absorption spectra of BPs-$FeSe_2$. **Figure S4.** Photographs of (a) $FeSe_2$, BPs and BPs-$FeSe_2$; (b) PEGylated $FeSe_2$, BPs and BPs-$FeSe_2$. **Figure S5.** The UV–vis absorption spectra of PEGylated $FeSe_2$, BPs and BPs-$FeSe_2$ solutions during 14 days. **Figure S6.** TEM images of BPs-$FeSe_2$-PEG under different pH conditions. **Figure S7.** Temperature curves of $FeSe_2$-PEG and BPs-PEG. **Figure S8.** Infrared thermal images and temperature change of BPs-$FeSe_2$-PEG in the 96-hole plate. **Figure S9.** The SVHUC-1 cell viability of PEGylated $FeSe_2$, BPs and BPs-$FeSe_2$ at various concentrations. **Figure S10.** Fluorescence images of EJ cells treated with coumarin-6-loaded BPs-$FeSe_2$-PEG. **Figure S11.** The changes of H_2O_2 level in EJ bladder cells under different treatment **Figure S12.** Photos of EJ bladder tumor-bearing mice with/without laser at different time points. **Figure S13.** Hematological analysis of mice. **Figure S14.** The in vivo biodistribution of Se concentration. **Figure S15.** Plasma Se concentration. **Table S1** Pharmacokinetic parameters of BP-$FeSe_2$-PEG.

Acknowledgements
Not applicable.

Authors' contributions
XD and HL participated in experiments, data analysis, manuscript writing and contributed equally in this investigation; YX carried out experiments, collected and analyzed data; LC carried out experiments; ZX carried out experiments; JX carried out experiments; ZT carried out experiments; FY supervised the entire project, involved in the designing of conceptual framework and wrote the manuscript; TC supervised the entire project, involved in the designing of conceptual framework and wrote the manuscript. All authors read and approved the final manuscript.

Funding
This work was supported by National Natural Science Foundation of China (21877049), Major Program for Tackling Key Problems of Industrial Technology in Guangzhou (201902020013), China Postdoctoral Science Foundation (2019M653279), Dedicated Fund for Promoting High-Quality Marine Economic Development in Guangdong Province (GDOE-2019-A31, 2020-035), Guangzhou Key Laboratory of Molecular and Functional Imaging for Clinical Translation (201905010003), Innovation Team Project in Guangdong Colleges and Universities (2019KCXTD008, 2019KTSCX012), Opening fund of Hubei Key Laboratory of Bioinorganic Chemistry & Materia Medica (BCMM202001), Guangdong Province Medical Research Fund (A2021033) and K. C. Wong Education Foundation.

Availability of data and materials
All data generated or analyzed during this study are included in this article.

Declarations

Ethics approval and consent to participate
The study had animal ethics approval from Jinan University Animal Ethics Committee. The manuscript does not contain clinical studies or patient data.

Consent for publication
All authors consent to publish.

Competing interests
The authors declared no competing financial interest.

Author details
[1]College of Chemistry and Materials Science, Guangdong Provincial Key Laboratory of Functional Supramolecular Coordination Materials and Applications, Jinan University, Guangzhou 510632, China. [2]Medical Imaging Center, The First Affiliated Hospital, Jinan University, Guangzhou 510632, China. [3]Department of Urology, Guangzhou Institute of Urology, Guangdong Key Laboratory of Urology, the First Affiliated Hospital of Guangzhou Medical University, Guangzhou Medical University, Guangzhou 510230, China.

Received: 23 March 2021 Accepted: 21 May 2021
Published online: 06 July 2021

References

1. Nuevo-Tapioles C, Santacatterina F, Stamatakis K, de Arenas CN, de Cedron MG, Formentini L, Cuezva JM. Coordinate beta-adrenergic inhibition of mitochondrial activity and angiogenesis arrest tumor growth. Nat Commun. 2020;111:3606.
2. Huang W, He L, Ouyang J, Chen Q, Liu C, Tao W, Chen T. Triangle-shaped tellurium nanostars potentiate radiotherapy by boosting checkpoint blockade immunotherapy. Matter. 2020;35:1725–53.
3. Liang P, Tang Q, Cai Y, Liu G, Si W, Shao J, Huang W, Zhang Q, Dong X. Self-quenched ferrocenyl diketopyrrolopyrrole organic nanoparticles with amplifying photothermal effect for cancer therapy. Chem Sci. 2017;811:7457–63.
4. Guo B, Sheng Z, Hu D, Li A, Xu S, Manghnani PN, Liu C, Guo L, Zheng H, Liu B. Molecular engineering of conjugated polymers for biocompatible organic nanoparticles with highly efficient photoacoustic and photothermal performance in cancer theranostics. ACS Nano. 2017;1110:10124–34.
5. Sun Q, He F, Bi H, Wang Z, Sun C, Li C, Xu J, Yang D, Wang X, Gai S, Yang P. An intelligent nanoplatform for simultaneously controlled chemo-, photothermal, and photodynamic therapies mediated by a single NIR light. Chem Eng J. 2019;362:679–91.
6. Ouyang J, Zhang L, Li L, Chen W, Tang Z, Ji X, Feng C, Tao N, Kong N, Chen T, Liu Y-N, Tao W. Cryogenic exfoliation of 2D stanene nanosheets for cancer theranostics. Nano-Micro Lett. 2021. https://doi.org/10.1007/s40820-021-00619-1.
7. Ji X, Ge L, Liu C, Tang Z, Xiao Y, Chen W, Lei Z, Gao W, Blake S, De D, Shi B, Zeng X, Kong N, Zhang X, Tao W. Capturing functional two-dimensional nanosheets from sandwich-structure vermiculite for cancer theranostics. Nat Commun. 2021;121:1124.
8. Liu C, Shin J, Son S, Choe Y, Farokhzad N, Tang Z, Xiao Y, Kong N, Xie T, Kim JS, Tao W. Pnictogens in medicinal chemistry: evolution from erstwhile drugs to emerging layered photonic nanomedicine. Chem Soc Rev. 2021;504:2260–79.
9. Sheng D, Liu T, Deng L, Zhang L, Li X, Xu J, Hao L, Li P, Ran H, Chen H, Wang Z. Perfluorooctyl bromide & indocyanine green co-loaded nanoliposomes for enhanced multimodal imaging-guided phototherapy. Biomaterials. 2018;165:1–13.
10. Chen P, Ma Y, Zheng Z, Wu C, Wang Y, Liang G. Facile syntheses of conjugated polymers for photothermal tumour therapy. Nat Commun. 2019;101:1192.
11. Sheng J, Zhang L, Deng L, Han Y, Wang L, He H, Liu Y-N. Fabrication of dopamine enveloped WO_{3-x} quantum dots as single-NIR laser activated

photonic nanodrug for synergistic photothermal/photodynamic therapy against cancer. Chem Eng J. 2020;383:123071.
12. Kalluru P, Vankayala R, Chiang CS, Hwang KC. Nano-graphene oxide-mediated in vivo fluorescence imaging and bimodal photodynamic and photothermal destruction of tumors. Biomaterials. 2016;95:1–10.
13. Wang J, Chang Y, Luo H, Jiang W, Xu L, Chen T, Zhu X. Designing immunogenic nanotherapeutics for photothermal-triggered immunotherapy involving reprogramming immunosuppression and activating systemic antitumor responses. Biomaterials. 2020;255:120153.
14. Wang X-M, Huang L, Wang Y-J, Xuan L, Li W-W, Tian L-J. Highly efficient near-infrared photothermal antibacterial membrane with incorporated biogenic CuSe nanoparticles. Chem Eng J. 2021;405:126711.
15. Lv K, Lin H, Qu F. Biodegradable hollow Co_3S_4@N-doped carbon as enhanced PTT/PDT agent for multimodal MR/thermal imaging and synergistic antitumor therapy. Chem Eng J. 2020;392:124555.
16. Mei C, Wang N, Zhu X, Wong K-H, Chen T. Photothermal-controlled nanotubes with surface charge flipping ability for precise synergistic therapy of triple-negative breast cancer. Adv Funct Mater. 2018;2845:1805225.
17. Lee HP, Gaharwar AK. Light-responsive inorganic biomaterials for biomedical applications. Adv Sci. 2020;717:2000863.
18. Zhang F, Liu Y, Lei J, Wang S, Ji X, Liu H, Yang Q. Metal-organic-framework-derived carbon nanostructures for site-specific dual-modality photothermal/photodynamic thrombus therapy. Adv Sci. 2019;617:1901378.
19. Xia F, Wang H, Jia Y. Rediscovering black phosphorus as an anisotropic layered material for optoelectronics and electronics. Nat Commun. 2014;5:4458.
20. Wang X, Cheng L. Multifunctional two-dimensional nanocomposites for photothermal-based combined cancer therapy. Nanoscale. 2019;1134:15685–708.
21. Sun J, Sun Y, Pasta M, Zhou G, Li Y, Liu W, Xiong F, Cui Y. Entrapment of polysulfides by a black-phosphorus-modified separator for lithium-sulfur batteries. Adv Mater. 2016;2844:9797–803.
22. Shao J, Xie H, Huang H, Li Z, Sun Z, Xu Y, Xiao Q, Yu XF, Zhao Y, Zhang H, Wang H, Chu PK. Biodegradable black phosphorus-based nanospheres for in vivo photothermal cancer therapy. Nat Commun. 2016;7:12967.
23. Qu G, Liu W, Zhao Y, Gao J, Xia T, Shi J, Hu L, Zhou W, Gao J, Wang H, Luo Q, Zhou Q, Liu S, Yu XF, Jiang G. Improved biocompatibility of black phosphorus nanosheets by chemical modification. Angew Chem Int Ed. 2017;5646:14488–93.
24. Ouyang J, Liu RY, Chen W, Liu Z, Xu Q, Zeng K, Deng L, Shen L, Liu YN. A black phosphorus based synergistic antibacterial platform against drug resistant bacteria. J Mater Chem B. 2018;639:6302–10.
25. Liang M, Zhang M, Yu S, Wu Q, Ma K, Chen Y, Liu X, Li C, Wang F. Silver-laden black phosphorus nanosheets for an efficient in vivo antimicrobial application. Small. 2020;1613:e1905938.
26. Li Z, Fu Q, Ye J, Ge X, Wang J, Song J, Yang H. Ag^+-coupled black phosphorus vesicles with emerging NIR-II Photoacoustic Imaging Performance For Cancer Immune-Dynamic Therapy And Fast Wound Healing. Angew Chem Int Ed. 2020;5949:22202–9.
27. Ouyang J, Deng Y, Chen W, Xu Q, Wang L, Liu Z, Tang F, Deng L, Liu YN. Marriage of artificial catalase and black phosphorus nanosheets for reinforced photodynamic antitumor therapy. J Mater Chem B. 2018;614:2057–64.
28. Xie J, Fan T, Kim JH, Xu Y, Wang Y, Liang W, Qiao L, Wu Z, Liu Q, Hu W. Emetine-loaded black phosphorus hydrogel sensitizes tumor to photothermal therapy through inhibition of stress granule formation. Adv Funct Mater. 2020;3043:2003891.
29. Huang J, He B, Zhang Z, Li Y, Kang M, Wang Y, Li K, Wang D, Tang BZ. Aggregation-induced emission luminogens married to 2D black phosphorus nanosheets for highly efficient multimodal theranostics. Adv Mater. 2020;3237:e2003382.
30. Yang X, Liu R, Zhong Z, Huang H, Shao J, Xie X, Zhang Y, Wang W, Dong X. Platinum nanoenzyme functionalized black phosphorus nanosheets for photothermal and enhanced-photodynamic therapy. Chem Eng J. 2021;409:127381.
31. Pan T, Fu W, Xin H, Geng S, Li Z, Cui H, Zhang Y, Chu PK, Zhou W, Yu XF. Calcium phosphate mineralized black phosphorous with enhanced functionality and anticancer bioactivity. Adv Funct Mater. 2020;3038:2003069.
32. Chen W, Ouyang J, Yi X, Xu Y, Niu C, Zhang W, Wang L, Sheng J, Deng L, Liu YN, Guo S. Black phosphorus nanosheets as a neuroprotective nanomedicine for neurodegenerative disorder therapy. Adv Mater. 2018. https://doi.org/10.1002/adma.201703458.
33. Wang Z, Zhao J, Tang W, Hu L, Chen X, Su Y, Zou C, Wang J, Lu WW, Zhen W, Zhang R, Yang D, Peng S. Multifunctional nanoengineered hydrogels consisting of black phosphorus nanosheets upregulate bone formation. Small. 2019;1541:e1901560.
34. Zhou Q, Chen Q, Tong Y, Wang J. Light-induced ambient degradation of few-layer black phosphorus: mechanism and protection. Angew Chem Int Ed. 2016;5538:11437–41.
35. Hanlon D, Backes C, Doherty E, Cucinotta CS, Berner NC, Boland C, Lee K, Harvey A, Lynch P, Gholamvand Z. Liquid exfoliation of solvent-stabilized few-layer black phosphorus for applications beyond electronics. Nat Commun. 2015;61:1–11.
36. Koda DS, Bechstedt F, Marques M, Teles LK. Tuning electronic properties and band alignments of phosphorene combined with $MoSe_2$ and WSe_2. J Mater Chem C. 2017;1217:3862–9.
37. Wang J, Liu D, Huang H, Yang N, Yu B, Wen M, Wang X, Chu PK, Yu XF. In-plane black phosphorus/dicobalt phosphide heterostructure for efficient electrocatalysis. Angew Chem Int Ed. 2018;5710:2600–4.
38. Edmonds MT, Tadich A, Carvalho A, Ziletti A, O'Donnell KM, Koenig SP, Coker DF, Ozyilmaz B, Neto AH, Fuhrer MS. Creating a stable oxide at the surface of black phosphorus. ACS Appl Mater Interfaces. 2015;727:14557–62.
39. Guo T, Lin Y, Jin G, Weng R, Song J, Liu X, Huang G, Hou L, Yang H. Manganese-phenolic network-coated black phosphorus nanosheets for theranostics combining magnetic resonance/photoacoustic dual-modal imaging and photothermal therapy. Chem Commun. 2019;556:850–3.
40. Yang X, Wang D, Shi Y, Zou J, Zhao Q, Zhang Q, Huang W, Shao J, Xie X, Dong X. Black phosphorus nanosheets immobilizing Ce6 for imaging-guided photothermal/photodynamic cancer therapy. ACS Appl Mater Interfaces. 2018;1015:12431–40.
41. Zhang Q, Wang W, Zhang M, Wu F, Zheng T, Sheng B, Liu Y, Shen J, Zhou N, Sun Y. A theranostic nanocomposite with integrated black phosphorus nanosheet, Fe_3O_4@MnO_2-doped upconversion nanoparticles and chlorin for simultaneous multimodal imaging, highly efficient photodynamic and photothermal therapy. Chem Eng J. 2020;391:123525.
42. Wu Q, Chen G, Gong K, Wang J, Ge X, Liu X, Guo S, Wang F. MnO_2-laden black phosphorus for mri-guided synergistic PDT, PTT, and chemotherapy. Matter. 2019;12:496–512.
43. Xu M, Yang G, Bi H, Xu J, Dong S, Jia T, Wang Z, Zhao R, Sun Q, Gai S, He F, Yang D, Yang P. An intelligent nanoplatform for imaging-guided photodynamic/photothermal/chemo-therapy based on upconversion nanoparticles and CuS integrated black phosphorus. Chem Eng J. 2020;382:122822.
44. Hu K, Xie L, Zhang Y, Hanyu M, Yang Z, Nagatsu K, Suzuki H, Ouyang J, Ji X, Wei J, Xu H, Farokhzad OC, Liang SH, Wang L, Tao W, Zhang MR. Marriage of black phosphorus and Cu^{2+} as effective photothermal agents for PET-guided combination cancer therapy. Nat Commun. 2020;111:2778.
45. Yang Y, Wang Y, Xu L, Chen T. Dual-functional Se/Fe complex facilitates TRAIL treatment against resistant tumor cells via modulating cellular endoplasmic reticulum stress. Chin Chem Lett. 2020;317:1801–6.
46. Liu H, Lin W, He L, Chen T. Radiosensitive core/satellite ternary heteronanostructure for multimodal imaging-guided synergistic cancer radiotherapy. Biomaterials. 2020;226:119545.
47. Fang X, Wu X, Li Z, Jiang L, Lo WS, Chen G, Gu Y, Wong WT. Biomimetic anti-PD-1 peptide-loaded 2D FePSe3 Nanosheets for efficient photothermal and enhanced immune therapy with multimodal MR/PA/thermal imaging. Adv Sci. 2020. https://doi.org/10.1002/advs.202003041.
48. Zhang P, Hou Y, Zeng J, Li Y, Wang Z, Zhu R, Ma T, Gao M. Coordinatively unsaturated Fe^{3+} based activatable probes for enhanced MRI and therapy of tumors. Angew Chem Int Ed. 2019;5832:11088–96.
49. Shi W, Zhang X, Che G, Fan W, Liu C. Controlled hydrothermal synthesis and magnetic properties of three-dimensional $FeSe_2$ rod clusters and microspheres. Chem Eng J. 2013;215–216:508–16.
50. Liu Y, Yang C, Li Y, Zheng F, Li Y, Deng Q, Zhong W, Wang G, Liu T. $FeSe_2$/nitrogen-doped carbon as anode material for potassium-ion batteries. Chem Eng J. 2020;393:124590.
51. Qin Z, Yang BC, Zhang SR, Li K, Yan SQ, Lv XW, Li ZJ. Flower-like pyrite $FeSe_2$ nanoparticles with enhanced optical properties by hot-injection. Vacuum. 2015;111:157–9.

52. Kang M, Chen F, Wu S, Yang Y, Bruggeman C, Charlet L. Effect of pH on aqueous Se(IV) reduction by pyrite. Environ Sci Technol. 2011;457:2704–10.
53. Huang H, He L, Zhou W, Qu G, Wang J, Yang N, Gao J, Chen T, Chu PK, Yu XF. Stable black phosphorus/Bi_2O_3 heterostructures for synergistic cancer radiotherapy. Biomaterials. 2018;171:12–22.
54. Chan L, Chen X, Gao P, Xie J, Zhang Z, Zhao J, Chen T. Coordination-driven enhancement of radiosensitization by black phosphorus via regulating tumor metabolism. ACS Nano. 2021. https://doi.org/10.1021/acsnano.0c09454.
55. Fu T, Chen Y, Hao J, Wang X, Liu G, Li Y, Liu Z, Cheng L. Facile preparation of uniform $FeSe_2$ nanoparticles for PA/MR dual-modal imaging and photothermal cancer therapy. Nanoscale. 2015;748:20757–68.
56. Liu T, Lai L, Song Z, Chen T. A sequentially triggered nanosystem for precise drug delivery and simultaneous inhibition of cancer growth, migration, and invasion. Adv Funct Mater. 2016;2643:7775–90.
57. Brent JR, Savjani N, Lewis EA, Haigh SJ, Lewis DJ, O'Brien P. Production of few-layer phosphorene by liquid exfoliation of black phosphorus. Chem Commun. 2014;5087:13338–41.
58. Bao T, Yin W, Zheng X, Zhang X, Yu J, Dong X, Yong Y, Gao F, Yan L, Gu Z, Zhao Y. One-pot synthesis of PEGylated plasmonic MoO_{3-x} hollow nanospheres for photoacoustic imaging guided chemo-photothermal combinational therapy of cancer. Biomaterials. 2016;76:11–24.
59. Wang H, Mukherjee S, Yi J, Banerjee P, Chen Q, Zhou S. Biocompatible chitosan-carbon dot hybrid nanogels for NIR-imaging-guided synergistic photothermal-chemo therapy. ACS Appl Mater Interfaces. 2017;922:18639–49.
60. Yin WY, Yan L, Yu J, Tian G, Zhou LJ, Zheng XP, Zhang X, Yong Y, Li J, Gu ZJ, Zhao YL. High-throughput synthesis of single-layer MoS_2 nanosheets as a near-infrared photothermal-triggered drug delivery for effective cancer therapy. ACS Nano. 2014;87:6922–33.
61. Luo Y, Liu X, Tan L, Li Z, Yeung KWK, Zheng Y, Cui Z, Liang Y, Zhu S, Li C, Wang X, Wu S. Enhanced photocatalytic and photothermal properties of ecofriendly metal-organic framework heterojunction for rapid sterilization. Chem Eng J. 2021;405:126730.
62. Chang Y, He L, Li Z, Zeng L, Song Z, Li P, Chan L, You Y, Yu XF, Chu PK, Chen T. Designing core-shell gold and selenium nanocomposites for cancer radiochemotherapy. ACS Nano. 2017;115:4848–58.
63. Roch A, Gossuin Y, Muller RN, Gillis P. Superparamagnetic colloid suspensions: water magnetic relaxation and clustering. J Magn Magn Mater. 2005;2931:532–9.
64. Matsumoto Y, Jasanoff A. T_2 relaxation induced by clusters of superparamagnetic nanoparticles: Monte Carlo simulations. Magn Reson Imaging. 2008;267:994–8.
65. Tong S, Hou S, Zheng Z, Zhou J, Bao G. Coating optimization of superparamagnetic iron oxide nanoparticles for high T_2 relaxivity. Nano Lett. 2010;1011:4607–13.
66. Vuong QL, Gillis P, Gossuin Y. Monte Carlo simulation and theory of proton NMR transverse relaxation induced by aggregation of magnetic particles used as MRI contrast agents. J Magn Reson. 2011;2121:139–48.
67. Pöselt E, Kloust H, Tromsdorf U, Janschel M, Hahn C, Maßlo C, Weller H. Relaxivity optimization of a PEGylated iron-oxide-based negative magnetic resonance contrast agent for T_2-weighted spin–echo imaging. ACS Nano. 2012;62:1619–24.
68. Tadic M, Kralj S, Jagodic M, Hanzel D, Makovec D. Magnetic properties of novel superparamagnetic iron oxide nanoclusters and their peculiarity under annealing treatment. Appl Surf Sci. 2014;322:255–64.
69. Atanasijevic T, Shusteff M, Fam P, Jasanoff A. Calcium-sensitive MRI contrast agents based on superparamagnetic iron oxide nanoparticles and calmodulin. PNAS. 2006;10340:14707–12.
70. Shaw PH. The role of p53 in cell cycle regulation. Pathol Res Pract. 1996;1927:669–75.
71. He L, Huang G, Liu H, Sang C, Liu X, Chen T. Highly bioactive zeolitic imidazolate framework-8–capped nanotherapeutics for efficient reversal of reperfusion-induced injury in ischemic stroke. Science Adv. 2020;612:eaay9751.

Publisher's Note